CHALMERS

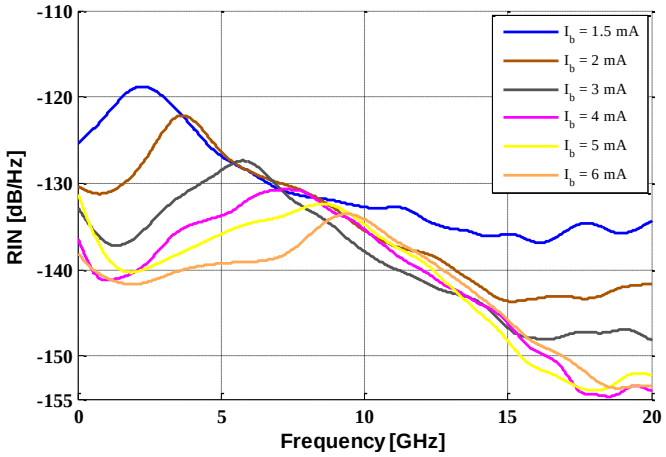



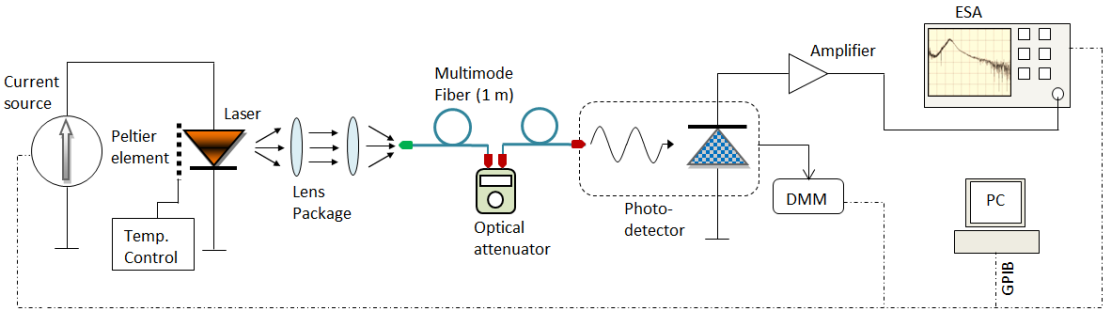


# Relative Intensity Noise (RIN) in High-Speed VCSELs for Short Reach Communication

*Master of Science Thesis in Photonics Engineering*

SEYED EHSAN HASHEMI

*Photonics Laboratory*
*Department of Microtechnology and Nanoscience (MC2)*
CHALMERS UNIVERSITY OF TECHNOLOGY
Göteborg, Sweden, 2012

**Thesis for the degree of Master of Science**

# Relative Intensity Noise (RIN) in High Speed Vertical Cavity Surface Emitting Lasers for Short Reach Communication

Seyed Ehsan Hashemi


Photonics Laboratory
*Department of Microtechnology and Nanoscience (MC2)*
CHALMERS UNIVERSITY OF TECHNOLOGY
Göteborg, Sweden 2012

Relative Intensity Noise (RIN) in High Speed VCSELs for Short Reach Communications

Seyed Ehsan Hashemi

Göteborg, March 2012



Photonics Laboratory
Department of Microtechnology and Nanoscience
Chalmers University of Technology

SE-412 96 Göteborg, Sweden
Telephone +46 (0)31 772 1000

Typeset using LyX

Cover: Example of RIN diagram of a VCSEL at different injection currents (Top-left), Microscope image of fully processed VCSEL on wafer [46] (Top-right), and the experimental setup for RIN measurement (Down).

Printed by Chalmers Reproservice
Göteborg, Sweden, March 2012

## Abstract

Lasers in the steady state condition do not provide constant carrier and photon densities even without any current modulation. These optical power variations provide an intensity noise. Since optical transmission systems have a critical impairment due to this noise source, it is quite important to know how it can be defined and measured. Relative intensity noise (RIN) is a measure in order to quantify and determine how noisy the laser, as the transmitter of transmission line, is. The work of this Master degree project has been both experimental and analytical. In the first experimental part of the project, relative intensity noise (RIN) was measured on state-of-the-art high-speed multi-mode 850-nm vertical-cavity surface-emitting lasers (VCSELs) intended for next generation short reach data communication standards. Measurements have been performed on devices with different current aperture diameters, at different bias currents, and at both room temperature (RT) and 85°C. The RIN values obtained are shown to be in most cases below the requirements, for example, in the future 32 Gb/s Fibre Channel (32GFC) standard. The second analysis part of the project dealt with extracting values of intrinsic dynamic laser parameters from RIN measurements and comparing to those extracted from corresponding $S_{21}$ measurements, which is the conventional method. Good agreement was found, and the pros and cons for the two extraction techniques are discussed.

Keywords: Relative-intensity-noise (RIN), vertical-cavity surface-emitting laser (VCSEL), high-speed multi-mode VCSEL, intensity noise measurement, VCSEL intensity noise, intrinsic dynamic parameters, $S_{21}$ measurement.

## Acknowledgment

First of all, many thanks go to all the people at the Photonics Laboratory for contributing to a very pleasant and stimulating atmosphere. I would like to thank Prof. Anders Larsson who made the possibility for me to work on this project and be a member of the lab. My exceptional gratitude goes to Dr. Johan Gustavsson for his insightful, supportive, and invaluable supervision. I am very thankful for his patience and vital guidance that always showed me the right direction. Dr. Petter Westbergh is also greatly appreciated for his crucial helps at different stages of the project.

I have been really amazed by how understanding and mature, people are at the Photonics Laboratory, especially when we had to share the measurement setup or the instruments. They have also been so caring that they never withheld their fruitful hints. Many thanks therefore go to Krzysztof Szczerba, Samuel Olsson, Erik Haglund, Dr. Bill Corcoran, and Dr. Benjamin Kögel. I also thank Dr. Åsa Haglund for her helpful tips regarding the presentation of my work.

I would like to acknowledge all my teachers and fellow students at the Wireless and Photonics Engineering program at Chalmers University of Technology and also during my bachelor's studies at the Electrical Engineering program at Amirkabir University of Technology in Tehran, Iran.

Last but not least, I am willing to express my deepest appreciation to my parents and my lovely brothers for their never-ending support, care, and passion, without whom I would have never made it to this point.

Ehsan Hashemi

*Göteborg*
*March 2012*

# List of Abbreviations

| | |
|---|---|
| AR | Anti Reflection |
| BER | Bit-Error Rate |
| DBR | Distributed Bragg Reflector |
| DFB | Distributed Feedback |
| DUT | Device Under Test |
| ESA | Electrical Spectrum Analyzer |
| FC | Fibre Channel |
| FIR | Finite Impulse Response |
| GbE | Gigabit Ethernet |
| Gbps | Gigabit Per Second |
| GSG | Ground-Source-Ground |
| HPC | High Performance Computing |
| LAN | Local Area Network |
| LNA | Low Noise Amplifier |
| MPN | Mode-Partitioning Noise |
| NA | Numerical Aperture |
| NF | Noise Figure |
| OMA | Optical Modulation Amplitude |
| OSA | Optical Spectrum Analyzer |
| PSD | Power Spectral Density |
| QW | Quantum Well |
| RBW | Resolution Bandwidth |
| RF | Radio Frequency |
| RIN | Relative Intensity Noise |
| RT | Room Temperature |
| SAN | Storage Area Network |
| SNR | Signal-to-Noise Ratio |

| | |
|---|---|
| VBW | Video Bandwidth |
| VCSEL | Vertical-Cavity Surface-Emitting Laser |
| VOA | Variable Optical Attenuator |
| WDM | Wavelength-Division Multiplexing |

# Contents

# 1 Introduction and motivation

In modern lightwave technologies, the demands on the optical transmitters and lasers are always increasing since they are one of the backbones of many efficient optical systems. In different applications, each portion of the laser can be very important and crucial. One of the most important applications where lasers play a great role, is optical fiber communication, in which the need of improving the data rates are increasing everyday. Also in some very precise measuring and sensing applications, lasers with high spectral purity, coherency, etc, are required.

In reality, lasers in the steady state condition, do not provide constant carrier and photon densities even without any current modulation. Random carrier and photon recombination and generation events produce instantaneous time fluctuations in the carrier and photon densities. Variations in photon densities result in output optical power variations which provides an intensity noise while the fluctuations in carrier density lead to frequency noise, or instability in the output wavelength, which creates a finite spectral linewidth for the lasing mode [1].

In many applications, information about the intensity noise spectrum is of high interest. First and foremost, in a transmission communication system, one needs to know the intensity noise characteristics of the laser diode because it affects the signal to noise ratio (SNR) of the link. Therefore, for boosting the data rate of the transmission system, a laser diode with a certain noise performance needs to be employed. In addition, RIN measurement of any laser provides some information related to the inherent parameters of the device such as relaxation oscillation frequency.

The motivation and background of this project originate from the semiconductor lasers developed and fabricated at the Photonics Laboratory of Chalmers University of Technology. Researchers in this group have realized state-of-the-art high speed vertical-cavity surface-emitting lasers (VCSELs) emitting at 850 nm wavelength. Since these lasers are primarily intended for future short-range communication standards using different modulation protocols, the intensity noise performance of these high speed devices has been very interesting to investigate in order to evaluate whether they meet the RIN specifications in these new standards.

Moreover, the information that can be extracted from measured RIN spectrum gives good insight in the intrinsic dynamic parameters of the device. This information is valuable when developing the next generation designs of this type of components. However, using RIN spectra for this purpose is not as common as using normal $S_{21}$ (modulation response) spectra, but the advantages of this method compared to the conventional $S_{21}$ method can be identified.

This report comprises of three parts. In the first part which consists of Chapters 2, 3 and 4, the theoretical knowledge required for this work is outlined. VCSEL structure and dynamics are highlighted since this work is dedicated to this special type of semiconductor lasers.

In the second part, which consists of Chapters 5 and 6, different RIN measurement techniques are explained in detail. Finally, the measurement results are shown for devices with different current aperture diameters, at different bias currents, and at both room temperature (RT) and $85°C$ ambient temperature. As annotated above, the measured RIN spectrum can also be used to study the intrinsic high frequency properties of the device, i.e., the relaxation oscillation frequency and damping factor of the VCSEL can be extracted from the RIN spectrum. Conventionally, these parameters are extracted from the small-signal intensity modulation response ($S_{21}$) of the laser. These two methods are analytically discussed and experimentally compared in Chapter 7.

In Chapter 8, a summary/conclusion of the work and future outlook is made.

# 2 VCSEL theory

## 2.1 Fundamentals of diode lasers

A semiconductor laser is a coherent light emitting source that utilizes semiconductor material to form the gain medium, in contrast to gas, dye, and other types of lasers. A very common type of semiconductor lasers is diode laser, in which the population inversion is established by driving current through the active medium (electrical pumping), whereas in the other types, the population inversion is accomplished by optical pumping.

Semiconductor lasers, in their simplest form, consist of layered structure of an undoped (intrinsic) direct-bandgap semiconductor material sandwiched between p- and n-doped cladding layers with higher bandgap. By forward biasing this p-i-n junction, electrons and holes are transported and accumulated in the active region (intrinsic layer). Thereby, by recombination of electron and hole pairs, radiative transitions can occur. By increasing the biasing current (stronger pumping), a certain point is reached, in which the optical field gain overcomes the optical field cavity losses during one round-trip and the device can start to lase. Cavity losses comprise loss from the mirrors (not 100% reflectivity) and internal losses such as absorption loss in the gain medium. This is the so called amplitude condition for lasing. Besides, there is another condition entitled phase condition for lasing. A laser needs a cavity to form a feedback for the amplified light. The phase of the optical field has to repeat itself after one round-trip in the cavity. This condition yields the resonance frequencies of the cavity [2].

## 2.2 VCSEL: features and applications

Vertical cavity surface emitting laser (VCSEL) is one of the most important types of semiconductor lasers. As it implies from the name, the optical cavity is vertically oriented to emit photons perpendicular to the surface of the layered structure. The optical feedback is provided by use of highly reflective distributed Bragg reflectors (DBRs) above and below the active region, which results in a very short resonator. It, therefore, has some interesting features that satisfy requirements from the industry: very small physical size, high information transport capacity and low production costs. The advantages of VCSEL compared to other types of semiconductor lasers can be summarized; it has a high-modulation bandwidth at low injection currents due to high photon density resulting from very short cavity ($\sim 1\mu m$). Besides, VCSEL can provide high efficiency at low output powers (in mW range), high reliability, and a high temperature operational range. The surface emission results in a circular output beam with low divergence, which favors an easy and efficient coupling to optical fibers. Additionally, It has a low power consumption as well as capability of on-wafer testing before dicing and packaging which reduces the fabrication costs dramatically [2].

Nowadays, VCSELs have extensive application in fiber optics communication, especially in short reach communications, while they are also being used in other applications such as absorption spectroscopy, data storage networks, optical mice, among others. Wavelength tunable VCSELs have also attracted a lot of interest due to their numerous use in wavelength-division multiplexing (WDM) optical communication systems, gas detection, and fiber Bragg-grating sensors [3].

## 2.3 VCSEL dynamics

### 2.3.1 Rate equations

In general, one makes use of rate equations to investigate the dynamic behavior of the photon-carrier interaction in a VCSEL, biased above threshold. A set of two coupled rate equations is often formulated to analyze the intrinsic dynamic behavior of semiconductor lasers. One equation expresses the carrier density in the active region, and the other accounts for the photon density of the lasing mode in the cavity. These "standard" rate equations are as follows [1, 2]:

$$\frac{dN}{dt} = \frac{\eta_i I}{qV_a} - (AN + BN^2 + CN^3) - \upsilon_g GS, \tag{2.1}$$

$$\frac{dS}{dt} = \Gamma \upsilon_g GS - \frac{S}{\tau_p} + \Gamma \beta BN^2, \tag{2.2}$$

where $N$ is the excess carrier density in the active region, $\eta_i$ the internal quantum efficiency (the fraction of injected current that generates carriers in the active region), $I$ the injected current, $q$ the elementary charge, $AN + BN^2 + CN^3$ the recombination rate from spontaneous and non-radiative recombinations ($A$ is the Shockley-Read-Hall recombination coefficient, $B$ the spontaneous emission coefficient, and $C$ the Auger recombination coefficient), $\upsilon_g$ the group velocity of the lasing mode, $G$ the material gain, $S$ the photon density of the lasing mode, $\tau_p$ the photon lifetime which is related to the cavity losses through $\tau_p^{-1} = \upsilon_g \cdot [\alpha_i + \alpha_m]$, and finally $\beta$ is the fraction of photons generated by spontaneous emission which goes into the lasing mode.

Unfortunately, exact analytical solutions to the rate equations beside the steady-state do not exist. However, if the perturbations from the steady-state value are small, a small signal analysis yields an approximate analytical solution.

### 2.3.2 Small signal modulation

By substituting some of the terms in the coupled rate equations by the first order Taylor expansion, we can investigate the small signal response of Eqs. 2.1 and 2.2 of one variable in terms of perturbation of another. These substitutions are: $I = I_b + \delta I$, $N = N_b + \delta N$, $S = S_b + \delta S$, and $G = g_b/(1 + \varepsilon S) + g_0 \delta N/(1 + \varepsilon S) - \varepsilon G \delta S/(1 + \varepsilon S)$. The subscript $b$ denotes that the expansion is around a biasing point $I_b$ above threshold [2]. Also, $\varepsilon$ is referred to as the gain compression factor [4], $g_b$ is equal to the threshold gain due to gain clamping above threshold, and $g_0$ is the nominal differential gain ($\partial g/\partial N$) at the bias point.

By setting the time derivatives of the steady-state quantities to zero, the consequent small signal equations become [2]:

$$\frac{d}{dt}\delta N = \frac{\eta_i}{qV_a}\delta I - \left[\frac{1}{\tau_{\Delta N}} + \frac{\upsilon_g g_0 S_b}{1 + \varepsilon S_b}\right]\delta N - \left[\frac{1}{\Gamma \tau_p} - \frac{\upsilon_g \varepsilon G S_b}{1 + \varepsilon S_b}\right]\delta S, \tag{2.3}$$

$$\frac{d}{dt}\delta S = \frac{\Gamma \upsilon_g g_0 S_b}{1 + \varepsilon S_b}\delta N - \frac{\Gamma \upsilon_g \varepsilon G S_b}{1 + \varepsilon S_b}\delta S, \tag{2.4}$$

where $1/\tau_{\Delta N} = A + 2BN_b + 3CN_b^2$, $\tau_{\Delta N}$ is the differential carrier lifetime, and the spontaneous emission factor ($\beta$) is neglected [2].

By manipulating the Eqs. 2.3 and 2.4 to eliminate $\delta N$, a second-order system equation appears:

$$\frac{d^2}{dt^2}\delta S + \gamma \frac{d}{dt}\delta S + 4\pi^2 f_r^2 \delta S = \frac{\eta_i}{qV_a}\frac{\Gamma \upsilon_g g_0 S_b}{1 + \varepsilon S_b}\delta I, \tag{2.5}$$

where the resonance frequency ($f_r$) and the damping factor ($\gamma$) are written as [2]:

$$f_r^2 = \frac{1}{4\pi^2}\left[\frac{1}{\tau_p}\frac{\upsilon_g g_0 S_b}{1+\varepsilon S_b} + \frac{1}{\tau_{\Delta N}}\frac{\Gamma\upsilon_g\varepsilon G S_b}{1+\varepsilon S_b}\right], \tag{2.6}$$

$$\gamma = \frac{\upsilon_g g_0 S_b}{1+\varepsilon S_b} + \frac{\Gamma\upsilon_g\varepsilon G S_b}{1+\varepsilon S_b} + \frac{1}{\tau_{\Delta N}}. \tag{2.7}$$

The modulation response can be obtained from a small sinusoidal current change $\delta I(t) = \delta I_0 e^{j2\pi ft}$. In equation 2.5, the photon density is substituted by a measurable quantity, i.e. optical output power via $P_{out} = \eta_0 hcSV_p/\lambda_0\tau_p$, where $V_p$ is the volume of the lasing mode and $\eta_0$ is the fraction of light that couples out from the cavity, known as optical efficiency. In order to get an expression for the sinusoidal modulation transfer function $H_i(f)$, we substitute $d/dt$ with $j2\pi f$ in equation 2.5, and assume $\delta S(t) = \delta S_0 e^{j2\pi ft}$ and $\delta P_{out}(t) = \delta P_0 e^{j2\pi ft}$ which results in [2]:

$$H_i(f) = \frac{\delta P_0}{\delta I_0} = \eta_d \frac{hc}{\lambda_0 q}\cdot\frac{f_r^2}{f_r^2 - f^2 + j\frac{f}{2\pi}\gamma}, \tag{2.8}$$

where $\eta_d = \eta_i\eta_o$ is the differential quantum efficiency.

Equation 2.8 is the intrinsic modulation transfer function of the VCSEL, representing a second order system with a resonance frequency $f_r$ and a damping factor $\gamma$. Thus, a damped resonance appears around the resonance frequency (See Fig. 2.1).

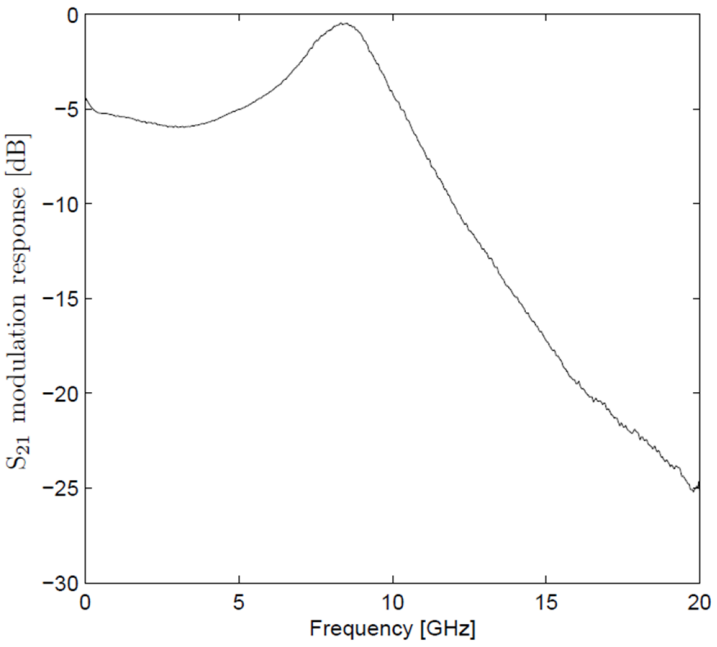


Figure 2.1: An example of the small signal modulation response ($S_{21}$) of a multi-mode VCSEL

In reality, the small signal modulation transfer function often contains an extra extrinsic contribution in the form of an extra pole. This is primarily caused by the parasitic capacitance of the laser and by carrier transport effects [5].

For the purpose of relating the impact of parasitics to the small signal modulation transfer function, the equivalent electrical circuit model of VCSEL, which is illustrated in Fig. 2.2 is often approximated by a simple RC-filter, represented by an additional pole with cut-off frequency $f_p$,

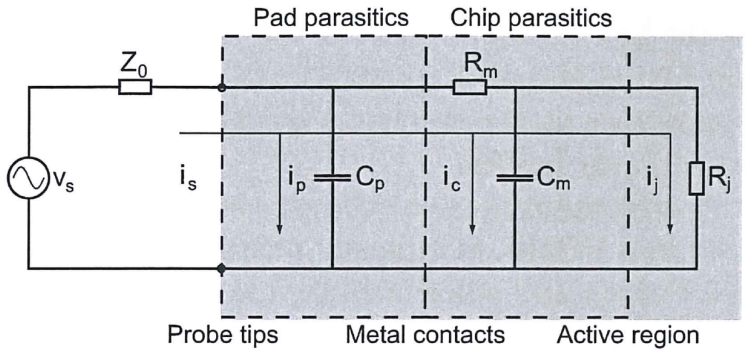


Figure 2.2: Small signal electrical model of VCSEL with driving source [2]

$$H_{par}(f) = \frac{1}{1 + j\frac{f}{f_p}}. \tag{2.9}$$

This additional term is multiplied by the intrinsic transfer function of VCSEL ($H_i(f)$), producing the total electrical transfer function ($H(f) = H_i(f) \cdot H_{par}(f)$) as [2]:

$$H(f) = C \cdot \frac{f_r^2}{f_r^2 - f^2 + j\frac{f}{2\pi}\gamma} \cdot \frac{1}{1 + j\frac{f}{f_p}}. \tag{2.10}$$

In the formula for the intrinsic modulation response in Eq. 2.8, we used an approximate expression for $f_r$,

$$f_r \approx \frac{1}{2\pi}\sqrt{\frac{\upsilon_g g_0 S_b}{\tau_p(1 + \varepsilon S_b)}}, \tag{2.11}$$

obtained by considering that $\tau_p \ll \tau_{\Delta N}$ and $g_0 \sim \Gamma\varepsilon G$ [1].
Using Eq. 2.11, the damping factor formula can be simplified to

$$\gamma \approx K \cdot f_r^2 + \gamma_0 \qquad \text{with} \qquad K = 4\pi^2\left[\tau_p + \frac{\varepsilon}{\upsilon_g g_0}\right], \tag{2.12}$$

where $\gamma_0 = 1/\tau_{\Delta N}$ is the damping factor offset and $K$ is the so-called $K$-factor.
The bandwidth of the laser has three different limitations, each of which is defined by one of the parameters in the denominator of Eq. 2.10 [5]. In order to reach the highest bandwidth, care must be taken in the design for both intrinsic and extrinsic limiting factors.

Eqs. 2.11 and 2.12 illustrate the intrinsic damping limitations of the laser. The resonance frequency increases as a function of the photon density as $f_r \propto \sqrt{S_b}$ (by increasing the injection current). On the other hand, the damping of the system increases at a faster pace since $\gamma \propto f_r^2 \propto S_b$, and will eventually limit the modulation bandwidth. If the extrinsic bandwidth limiting factors are neglected, the highest achievable intrinsic 3dB bandwidth in a semiconductor laser ($f_{3dB,max}$) is set by the $K$-factor and $\gamma_0$. By this assumption, the damping limited maximum bandwidth would be [2]:

$$f_{3dB,max} = f_{3dB,damping} \approx \frac{2\sqrt{2}\pi}{K} - \frac{\gamma_0}{2\sqrt{2}\pi} \tag{2.13}$$

However, extrinsic effects from self-heating and electrical parasitics tend to reduce the maximum bandwidth significantly and the damping limit is therefore seldom reached.

Beside $K$-factor, for actual devices, the so-called $D$-factor is another figure of merit. This intrinsic modulation factor quantifies the rate at which the resonance frequency increases with current. Its definition is as follows [2]:

$$D \equiv \frac{f_r}{\sqrt{I_b - I_{th}}} = \frac{1}{2\pi}\sqrt{\frac{\eta_i \Gamma v_g g_0}{qV_a}}, \tag{2.14}$$

where $I_{th}$is the threshold current.

The resonance frequency in VCSELs often saturates at high injection currents due to self-heating impairments of the device properties. The $D$-factor is therefore evaluated at low currents where both thermal effects and gain compression impacts are negligible [2].

## 2.4 Gen-II High speed VCSEL design

The work of this project has been performed on the "second generation" high-speed VCSEL designs emitting at 850 nm wavelength, fabricated at Chalmers University of Technology [2], being able to reach a record modulation bandwidth of 23 GHz for 850 nm multi-mode VCSELs [6]. Based on these VCSELs, an error-free transmission up to 40 Gbit/s was demonstrated by researchers at the Photonics Laboratory, Chalmers University of Technology; a record for 850 nm VCSELs [7].

The structure of this VCSEL is briefly mentioned here. Schematic view of this design can be seen in figure 2.3.

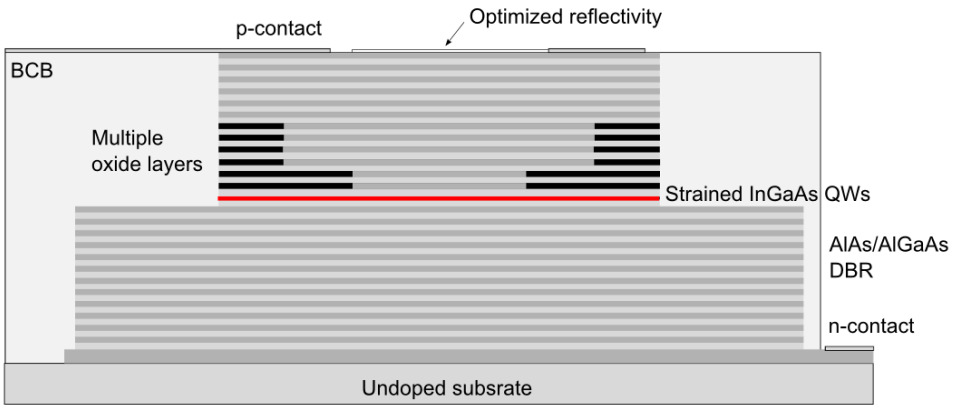


Figure 2.3: Schematic view of the high speed VCSEL design (Gen II) [8]

For this design, the goal was to identify factors that limit the modulation bandwidth of the device. Then each of these factors are treated to fade away as much as possible. These VCSELs employ an oxide confined structure in order to provide carrier confinement, while these oxide layers introduce parasitic capacitance, limiting the modulation performance of the device. In order to fabricate such oxide layers, layers with high Al-content is deposited during the epitaxial growth of DBR structure. After mesa etching, these high Al-content layers are exposed to a steam atmosphere at around $400°C$ by placing the wafer in the oxidation furnace. This oxidation process, converts the $Al_{0.98}GaAs$ layers to insulating oxide layers. Additionally, the oxide regions have lower refractive index, providing photon confinement. By introducing such an insulating layer, the injected current flows through the oxide apertures where the photon intensity is relatively high and good carrier confinement is thereby achieved. Compared to other methods, oxide confinement has become a standard and global technique. In the Gen-II type of VCSEL, a double oxide layer structure is used. But In order to suppress the parasitic capacitance induced by these oxide layers, four additional oxide layers are stacked above with a larger aperture. Introducing

too many of such large aperture oxide layers would increase the device resistivity too much. The Al-content in these oxide layers is 96%, while in the first two layers, it is 98%; therefore, it results in a narrower aperture [2].

The next consideration was to incorporate AlAs/$Al_{0.12}Ga_{0.88}As$ in bottom DBR for improved thermal conductivity. The reason for needing enhanced thermal conductivity is due to the fact that internal self-heating in VCSEL is one of the bandwidth limiting factors.

The next important factor is damping. If the modulation response of the device damps very quickly, then the bandwidth is reduced to a low value. Although this factor puts the ultimate limitation on the high-speed performance and it is usually difficult to reach this limit, but in this design all the other limiting factors were improved and it became necessary to address this issue. One of the most novel ideas in this design was, therefore, to reduce the photon lifetime. The idea to reduce the damping which corresponds to a lower $K$-factor, is that $K$-factor is linearly proportional to the photon lifetime $\tau_p$. Thus, by lowering down the photon lifetime one can reach a lower damping. There are different ways to reduce the photon lifetime, one is to shallow surface etch into the top DBR. In fact, the up-most layer of the top DBR, has a semiconductor/air interface, causing a large refractive index step. This makes a large reflection of the light. By etching the surface of the VCSEL, or by adding an anti-reflection (AR) coating on top of the surface (e.g. $Si_xN_y$or $\alpha$-Si), similar results will be achieved [8]. It should be mentioned that the chip of the VCSELs that were measured in this project, had 62 nm (corresponds to $\lambda/4$) $\alpha$-Si, deposited above the top DBR acting as an AR coating.

In order to reach the damping limited modulation bandwidth at low injection currents, before the thermal degradation, it is essential that the resonance frequency increases at a high rate with current. This translates into a high $D$-factor requirement. $D$-factor can be boosted by increasing the differential gain and reducing the threshold current density. In this design, the differential gain was enhanced by using strained quantum wells (QW). Healy et al [9], showed that by replacing standard GaAs/AlGaAs QWs with strained InGaAs/AlGaAs QWs, the $D$-factor was increased by 50%, due to a higher differential gain obtained from the strained QWs [2].

# 3 RIN theory

## 3.1 Definition of relative intensity noise (RIN)

In figure 3.1, the left figure illustrates the ideal output intensity of a laser, biased at a d.c. level while all the parameters influencing the laser, such as temperature, are assumed to be constant. On the other hand, the right figure shows the real case, when the output intensity of the laser shows power fluctuation due to *intensity noise*. In the definition of the relative intensity noise, the contribution of the intensity variations of the laser to the total electrical noise at the receiver is considered. This part of the electrical noise relative to the electrical signal power defines the RIN.

The measurement of RIN serves as a quality indicator of laser devices. It can be thought of as a type of inverse carrier-to-noise-ratio measurement [10]. Therefore, the higher the RIN value, the more noisy the laser and a higher power penalty from RIN is induced.

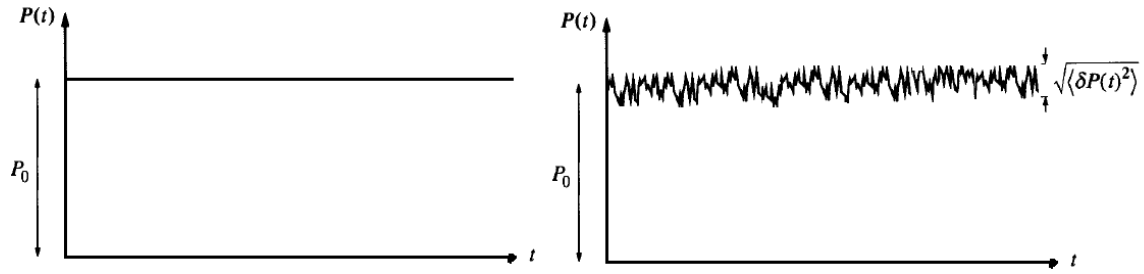


Figure 3.1: Left image is the ideal output power for a laser with dc bias, and the right image is the real laser output power having intensity noise.

The RIN definition in *linear* form is as follows; we assume that RIN is white noise (constant for all frequencies). Moreover, for convenience, RIN is always normalized to a 1–Hz bandwidth so that it becomes easier to compare the intensity fluctuations of the laser when receivers with different bandwidths are used [1]

$$RIN_{Lin} = \frac{< \delta P(t)^2 >}{P_0^2 \cdot \Delta f} \ [1/\text{Hz}], \tag{3.1}$$

where $\delta P(t)$ is the optical intensity fluctuations, the $<>$ denotes the time average, $P_0$ is the dc optical power, and $\Delta f$ is the noise bandwidth (detection system bandwidth).

Consequently, in dB unit, the definition of RIN is the ratio of the laser noise power normalized to 1–Hz bandwidth, and the average (or d.c.) power of the photocurrent- both considered in electrical domain [1]

$$RIN[\text{dB/Hz}] = 10\log(\frac{< \delta P(t)^2 >}{P_0^2})[\text{dB}] - 10\log(\Delta f[\text{Hz}]). \tag{3.2}$$

## 3.2 Intensity noise origin

The predominant source of RIN is *spontaneous emission* [1, 11, 12]. Lasers above their lasing threshold, mostly emit stimulated emission and also a small amount of spontaneous emission[1]. Since the spontaneous emission photons have random wavelength, polarization, direction, and phase, they can coincide with the wavelength and the direction of the stimulated emission photons and produce variations in the output intensity and output frequency of the laser[2] (See Fig. 3.2) [13].

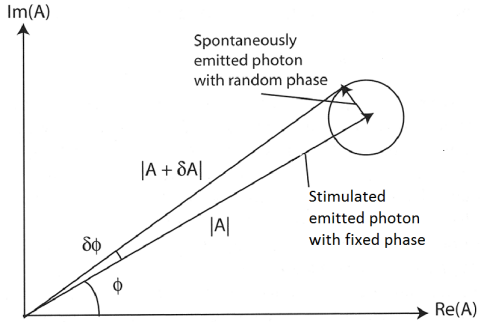


Figure 3.2: Phasor diagram illustrating intensity and phase noise due to spontaneous emission [15]

The spontaneous emission beats with the stimulated emissions above the threshold in a laser (The spontaneous-spontaneous beating component can be easily ignored compared to the stimulated-spontaneous one). Depending on the receiver properties in the photodetection process, this beating noise component is detectable if it exceeds the other noise sources in the receiver electronics, which are thermal noise, shot noise of photocurrent, noise from electrical amplifier, noise from electrical spectrum analyzer, etc. Therefore, it is more reasonable to define the intensity noise of the laser after converting it to the electrical domain [13].

In [16], the RIN origin is attributed to both spontaneous emission and carrier recombination processes, which is said to be dependent on structural parameters of semiconductor lasers.

## 3.3 Intensity noise spectrum

In reality, relative intensity noise is not white noise. The spectrum of the RIN can be written as $RIN(f) = 2S_P(f)/< P_0 >^2$, where $S_P(f)$ is the double-sided spectral density of the output power [14]. RIN is low at low-frequencies and gradually increases with frequency. It has a maximum at a certain point which is around the resonance frequency of the cavity, and then it decreases at higher frequencies. The typical shape of a VCSEL RIN spectrum is depicted in figure 3.3.

In the relaxation oscillation, there is a coupling effect between the carrier and photon densities. Thereby any increase in carrier density will increase the optical gain and consequently the photon density. On the other hand, this increase in photon density contributes to more consumption of carriers in the cavity. Thus, the optical gain saturates, which causes the photon density to decrease. This, in turn, increases the carrier density due to reduced saturation effect (See Fig. 3.4). This resonance process, so called relaxation oscillation, is strong for a specific frequency which is close to $f_r$ [12].

For the frequencies much higher than the relaxation oscillation frequency, this coupling effect gradually vanishes and becomes weak. Hence, the intensity noise spectrum increases with fre-

[1]The definition of the lasing threshold is when the stimulated emission exceeds the spontaneous emission.
[2]Intensity and Phase noise

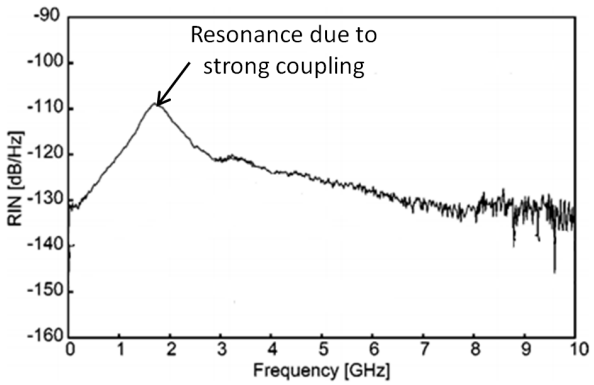


Figure 3.3: The typical shape of RIN spectrum for VCSELs

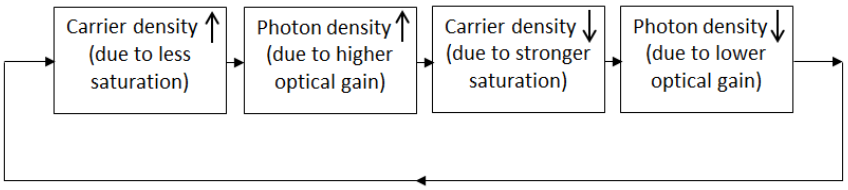


Figure 3.4: Explanation of relaxation oscillation process in a semiconductor laser

quency and has the peak around the resonance frequency, $f_r$, and it decreases again in higher frequencies.

## 3.4 RIN vs. injection current

In figure 3.5, RIN spectra are shown for a VCSEL at different bias currents. By increasing the bias current, the resonance frequency shifts to higher frequencies, while the response will be more damped. Moreover, the maximum RIN value which always occurs around the resonance frequency will be lower.

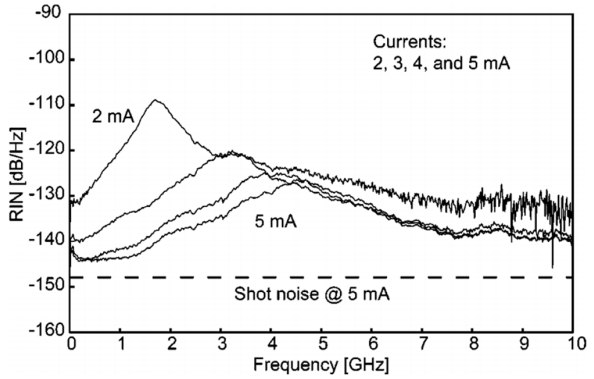


Figure 3.5: RIN spectra for different bias current for a VCSEL [5]

It is always more difficult to detect RIN at higher bias currents since the noise level is lower, which requires a detection system with much higher sensitivity. Eventually, the intensity noise becomes equal to the shot noise limit.

## 3.5 Intensity noise modification

Laser RIN depends on many quantities, the most important of which are frequency, output power, temperature, modulation frequency, time delay and magnitude of optical feedback, mode-suppression ratio, and relaxation oscillation frequency [17].

The effect of optical feedback (reflections) from the connectors and reflectors makes an external cavity that modifies the intensity noise. This feedback-induced intensity noise has periodical resonance peaks with the period of $\Delta f = \mathrm{c}/(2\mathrm{nL})$, where $L$ is the optical length of the external cavity, $n$ is the refractive index, and $c$ is the speed of light [12]. Yet, light can be reflected from some external facets which have polarization or wavelength-selective properties. For certain kinds of multi-mode lasers, RIN can also be affected significantly by system components that have polarization or wavelength-selective properties [10].

Dependence of RIN on frequency and output power was discussed earlier in this chapter. In multi-mode lasers, mode competition effects can result in higher RIN values especially at lower frequencies ($<$ 2GHz) [18, 19, 20]. VCSELs usually have large active diameters, allowing for multiple transverse-mode emission. Multi-transverse-mode operation ensures low source coherence, greatly minimizing interference effects like the modal noise-induced bit-error-rate in multi-mode fiber systems [21]. These mode competition effects will be discussed specifically in multi-mode VCSELs in Section 6.1.

The effect of phase noise to intensity noise conversion for distributed feedback lasers (DFB) have been discussed in [22] and [23]. This has been attributed to interferometric conversion of laser phase noise to intensity noise by multiple reflections at connectors and splices. Additionally, if the transmission system has chromatic-dispersive properties, it will also cause frequency noise to intensity noise conversion [24].

## 3.6 RIN transfer function

The frequency dependence of the intensity noise can be analytically identified by investigating how the spontaneous emission affects the characteristics of the laser. In order to do that, Langevin sources are added to the rate equations (as described in Section 2.3.1), to mathematically model the spontaneous emission [1, 25]. With this procedure, the transfer function describing the RIN attains the following form [5]:

$$RIN(f) = \frac{Af^2 + B}{(f_r^2 - f^2)^2 + (\frac{\gamma}{2\pi})^2 f^2}, \tag{3.3}$$

where $A$ and $B$ are terms dependent on the Langevin noise sources.

It is very interesting to observe that Eq. 3.3 has exactly the same denominator term as the absolute value of the intrinsic modulation response $|H_i(f)|$ (Eq. 2.8). Evidently, the intensity noise spectrum has the same general shape as the intrinsic modulation response, except for the frequency-squared term in the numerator that indicates the comparatively low noise levels at low frequencies and increased noise contributions at high frequencies [25].

# 4 System impairment due to RIN

The quality and performance of optical communication systems are, to a great extent, related to the properties of the laser source that is used. The important characteristics of lasers such as optical power, wavelength, spectral linewidth, modulation response, relative intensity noise, and modulation chirp are of great concern. Some of them have a fairly simple definition and can be measured rather straightforwardly, such as the output power or wavelength. However, measurement of some properties of the semiconductor lasers, such as relative intensity noise in this case, require a good understanding of the underlying physical mechanisms and the limitations which exist in the measurement techniques [12].

In figure 4.1, a noisy output power for both analog and digital signal transmission is depicted. For analog applications, SNR (signal-to-noise ratio) is used to quantify the quality of the signal with respect to the noise. Thus, excess noise can make it hard for the system to reach a certain required SNR. For digital applications, without taking the noise into consideration, a decision level at the midpoint, defines whether a '0' or '1' is detected. However, noise in digital signals can cause errors at the decision level. A certain amount of noise from the laser can thus be acceptable in order to satisfy the bit-error-rate (BER) criteria which typically is less than one in $10^9$ [1].

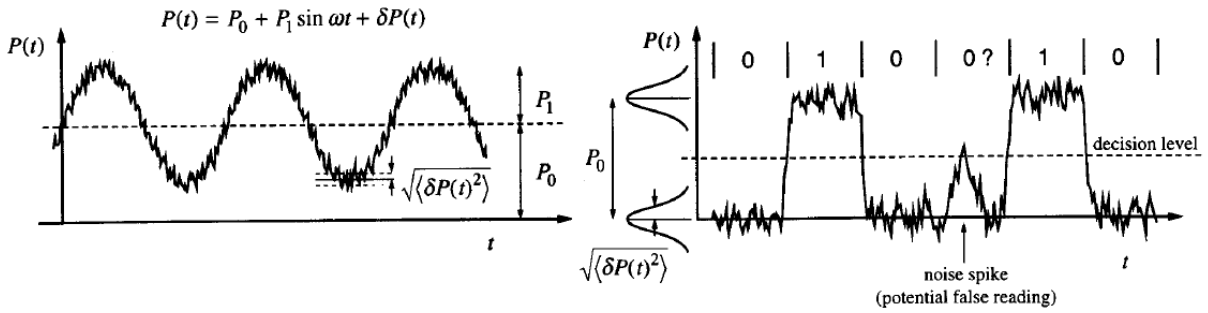


Figure 4.1: Noise in modulated laser signals for both analog (left) and digital applications (right) [1]

Practically, RIN is a very convenient parameter in the optical system performance calculation, as mentioned earlier, in analog systems, by defining the SNR through the RIN, or in digital systems, relating it to the BER will lead us to know the quality of the transmission line. If RIN is the only noise of source, the electrical signal to noise ratio can be defined by [1]

$$SNR = \frac{m^2}{2}\frac{1}{RIN_{TOT}}, \tag{4.1}$$

$$RIN_{TOT} = \int_0^{\Delta f} RIN(f) \cdot df, \tag{4.2}$$

where $m$ is the modulation index and $\Delta f$ is the receiver bandwidth [13, 1].

Modulation index ($m$) or depth of modulation can be defined as a measure of the extent of amplitude variation over an unmodulated carrier [26].

## 4.1 Estimating the RIN-induced power penalty for digital systems

We can estimate the noise ratio term from the following expression [27]:

$$\sigma = \sqrt{RIN_{TOT}} = \sqrt{\Delta f \cdot 10^{RIN/10}}, \tag{4.3}$$

where $\sigma$ is the noise ratio term without any dimension and RIN is expressed in dB/Hz units. More accurate equations for calculating the noise power ratio resulting from RIN exist in [42] and [28], but equation 4.3 is considered adequate for demonstration here.

The desired BER is often defined in terms of the Q factor. Q is expressed by this formula [29]:

$$Q = \frac{(I_{one} - I_{zero})}{(\sigma_{one} + \sigma_{zero})}, \tag{4.4}$$

where $I_{one}$ and $I_{zero}$ are the photocurrents corresponding to the logic one and logic zero optical power levels in amps unit, and $\sigma_{one}$ [A] and $\sigma_{zero}$ [A] are the corresponding rms noise currents in amps unit. (Note that $\sigma$ [-] in Eq. 4.3 is a relative noise current value and should not be mixed with $\sigma_{one}$ and $\sigma_{zero}$ parameters in Eq. 4.4.)

Usually, a BER of $10^{-12}$ is required in a link to have an "error free" transmission, which corresponds to a Q of about 7.

A RIN power penalty ($P_{rin}$) in dB can be stated as a function of Q factor and the total RIN-noise computed in equation 4.3, as follows [27]:

$$P_{rin} = 10 \cdot log\left(\sqrt{\frac{1}{1 - (Q \cdot \sigma)^2}}\right) \tag{4.5}$$

For example, given a RIN value of $-120$ dB/Hz, a Q factor of 7 and a receiver bandwidth of 20 GHz using equation 4.3, we obtain a value of 0.141 (dimensionless) for $\sigma$ and 0.85 dB for RIN-induced power penalty. This means that this amount of transmit power must be increased to compensate for the presence of the RIN.

# 5 RIN measurement

RIN is often measured in the electrical domain by direct detection. A photodetector is then used to convert the optical noise power into an electrical signal. The spectrum of this electrical noise signal is the target of the measurement. Obviously, an electrical spectrum analyzer (ESA) is the critical instrument in this case. Since the output photocurrent from the detector is usually a weak signal, electrical microwave amplifiers are needed to be placed after the detector. This amplification should be high enough to meet the sensitivity of the ESA [10]. However, the experiment is not as simple as this. In reality, RIN measurement has some limitations, therefore these limitations need to be specified and compensated. There are different techniques to overcome these limitations, which are going to be discussed in this chapter.

## 5.1 Experimental setup

In figure 5.1, the typical setup for measuring RIN is illustrated. In this setup, the idea is to detect the light using a photodetector, and then split the ac (noise) and the dc terms of the photocurrent.

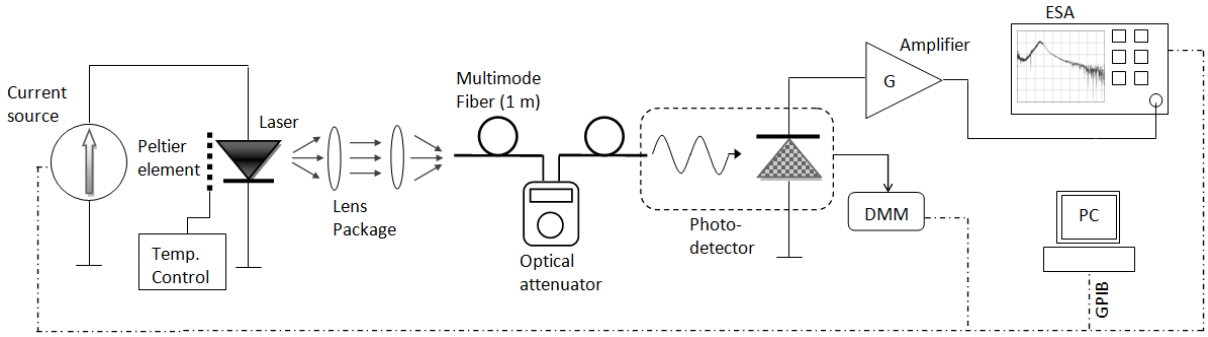


Figure 5.1: Experimental setup for measuring RIN (Employed in this project)

### 5.1.1 Biasing the laser at an elevated temperature

As it can be seen in the schematic of the setup for RIN measurement in figure 5.1, the semiconductor laser is biased by the current source, above the threshold current, using a *Yokogawa 7651* programmable d.c. source. Current is fed to the VCSEL through a high speed RF probe (*Picosecond* 40A-GSG-100-P from *GGB Industries*). A Peltier element and a thermistor are attached to the VCSEL sub-mount to enable measurements at elevated temperatures.

### 5.1.2 Optical coupling

The output light of the laser is coupled to a 50 $\mu m$ multi-mode fiber (1 m long) via an AR coated lens package. The divergent beam from VCSEL is collimated with a large numerical aperture (NA) lens and then focused with a smaller NA lens that matches the NA of the multi-mode fiber. This coupling system produces >60% coupling efficiency and minimizes optical feedback to the laser. For suppressing the reflections from the tip of the fiber, fibers having a tip which is

cut at an angle (12°) is used. Moreover, The fiber tip is further held at a slight angle, to reduce the possible reflections back to the laser. The fiber is connected to the photodetector. The high speed photodetector which is needed for these high speed lasers would typically have a rather small area. Consequently, to have a very precise measurement, it is very critical that the output light of the laser, can be captured completely and be sent through a fiber, to hit the effective area of the photodetector [30]. A *New Focus 1481-S-50 25* GHz fiber-coupled multi-mode detector was used in this project. Since the maximum input power to the photodetector was 2 mW, a variable optical attenuator (VOA) is placed in front of detector. In practice, it was observed that even if the output power is not beyond the limit, the usage of VOA improves the reduction of reflections, due to suppression of reflected light from the surface of the detector.

### 5.1.3 Handling the photocurrent

After the photodetector, we need to split the a.c. and d.c. terms of the photocurrent. The a.c. signal should be amplified to be detectable by the ESA; while the d.c. photocurrent should be connected to a digital multimeter to measure the average power of the detected light. The *New Focus* photodetector used in this project, has a bias monitor which shows the average voltage of the detected light. The average photocurrent can be calculated by considering a gain factor of 1 mV/$\mu$A. This bias monitor connector of the photodetector is linked to a *Keithley 2000* multimeter. Furthermore, the a.c. signal needs to be amplified and fed to an electrical spectrum analyzer (ESA). Two available broadband amplifiers were *SHF 100 AP,* 25 GHz bandwidth having 19 dB gain and *SHF 115 AP,* 20 GHz bandwidth having 27 dB gain. If one stage of amplification is needed, it is better to use the amplifier having the higher gain. Therefore, for most of the measurements in this project, *SHF 115* was used. This amplifier has around 6 dB noise figure which is acceptable. However, if the intensity noise is too low and higher sensitivity is required, these two amplifiers are used in cascade. Although this helps to increase the sensitivity of the system, the total gain will be much more fluctuating in frequency. These fluctuations in the total gain spectrum of the two amplifiers will cause fluctuations in the RIN trace, if gain compensation is not carried out carefully. Consequently, it was preferred to use only one stage of amplification. A d.c. block unit can be placed between the photodetector and the amplifier to filter out the large d.c. term from the output current of the photodetector, which might otherwise have saturation effects on the amplifier. Finally, an *Agilent E4440A* PSA series electrical spectrum analyzer was employed to measure the spectrum of the amplified a.c. signal, which is regarded as the total noise term.

## 5.2 RIN measurement limitations

In practice, extra noise sources are added to the pure laser intensity noise, from each of these electrical components that are used. Dark current from the photodetector, *thermal noise* from the electrical components such as amplifiers and ESA are the additional sources that mix with the laser intensity noise. Moreover, there is another noise source corresponding to the quantum nature of the light, the so called *shot noise*.

### 5.2.1 Total detected noise

What we measure on the electrical spectrum analyzer (ESA) is the total noise power, which is the summation of the above-mentioned noise sources (all are per Hz) [10]

$$N_{TOT}(f) = N_{Laser}(f) + N_{Shot} + N_{Thermal}(f)[\mathrm{W/Hz}]. \tag{5.1}$$

Considering thermal noise and shot noise in the photodetector and thermal noise in the electrical preamplifier, the RIN measured at the electrical spectrum analyzer can be expressed as [12]

$$RIN = \frac{S_p + \sigma_{shot}^2 + \sigma_{th}^2 + \sigma_{amp}^2}{\Re^2 P_{opt}^2} = RIN_{laser} + RIN_{error}, \tag{5.2}$$

In equation 5.2, $RIN$ is defined in dB/Hz unit, $S_p$ is the power spectral density of the intensity noise of laser which contributes to the RIN value; Other terms are regarded as *errors*. These different noise sources are investigated below.

### 5.2.2 Thermal noise

All the electronics including the load resistance, amplifiers, etc, which follow the photodetector produce thermal noise. The thermal noise does not depend on the optical power and is a constant value with frequency, which can be calculated and simply subtracted from the total noise. It only depends on the equivalent temperature of the electrical circuit, the load impedance and electrical bandwidth of the detection system. Thermal noise limits the sensitivity of the receiver and limits the maximum distance between the transmitter and the receiver in both analog and digital systems. To reduce the thermal noise contribution, very low noise amplifiers (LNA) are added after the photodetector. Because typical spectrum analyzers have 30 dB noise figure, thus by placing an LNA in between, the cascaded system would have a lower effective noise figure and problems caused by thermal noise will be reduced (Fig. 5.2). Typical noise figures for the amplifiers range from a few dB for narrow band amplifiers, 6 to 10 dB for low noise, wider band amplifiers, to as much as 15 dB. As it is clear, there is a trade off between a low noise and a wideband amplifier [10].

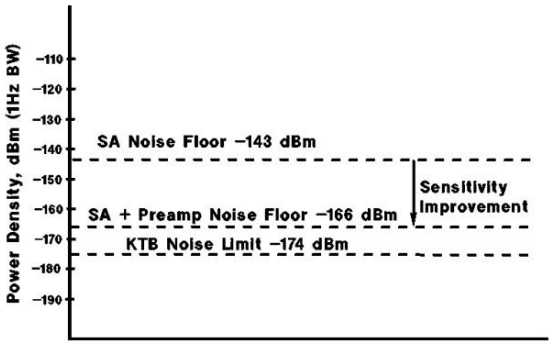


Figure 5.2: Noise limits in electrical systems are improved with a preamplifier [10]

$$\sigma_{Th}^2 = \frac{4K_B T}{R_L}\Delta f \ [A^2], \tag{5.3}$$

where $K_B$ is Boltzmann constant, $T$ is the temperature in Kelvin, and $R_L$ is the load resistance.

### 5.2.3 Shot noise

Shot noise is produced by the quantum nature of photons arriving at the detector, and related detection statistics. The noise produced is related directly to the amount of light incident on the photodetector (See Fig. 5.3) [10].

$$\sigma_{Shot}^2 = 2qI_{dc}\Delta f = 2q\Re P_0 \Delta f \ [A^2], \tag{5.4}$$

where $\Re$ is the responsivity of the photodiode, $P_0$ the optical power, and $q$ is the electron charge.

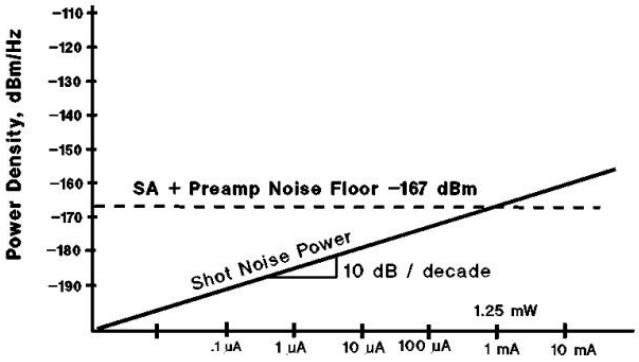


Figure 5.3: Shot noise increases with average power and can become larger than the thermal noise [10].

### 5.2.4 Intensity noise

Laser intensity noise, $N_{Laser}$, refers to the noise generated by the laser. The intensity noise source, contribution and modifications have been discussed already in chapter 3. The variance of output power fluctuations is written as [29]

$$\sigma^2_{Laser} = \Re^2 < (\Delta P_0^2) >= \Re^2 \cdot P_0^2 \cdot RIN_{TOT}. \tag{5.5}$$

As mentioned already $RIN_{TOT}$ is simply the inverse of the SNR of light emitted by the laser. $< (\Delta P_0^2) >$ is the average of optical power fluctuations.

### 5.2.5 Error term

Finally, if we plug-in the error terms, the final error term will be:

$$RIN_{error} = \frac{2q\Re P_{opt}}{\Re^2 P_{opt}^2} + \frac{K_B T(F_A G_A + F_{ESA} - 1)/G_A}{\Re^2 P_{opt}^2} + \frac{4K_B T/R_L}{\Re^2 P_{opt}^2}. \tag{5.6}$$

In equation 5.6, the first term is the relative shot noise power spectral density (PSD) of the photodetector, which is linearly proportional to the optical power; the second term is the equivalent relative thermal noise PSD, introduced by the electrical preamplifier and the electrical spectrum analyzer. The final term also represents the thermal noise of the photodetector. $F_A$ is the noise figure of the electrical preamplifier, $F_{ESA}$ the noise figure of the spectrum analyzer, and $G_A$ is the gain of the amplifier. Other parameters are already defined.

Figure 5.4 is a plot of $RIN_{Laser}$ against $RIN_{TOT}$ to show the effect of subtracting the thermal and shot noise with varying average power, assuming a fixed value of thermal noise (8 dB NF) and responsivity (0.8 A/W or 40 V/W into 50 ohms). The figure shows that when the total measured noise is greater than the thermal and shot noise terms by about 5 to 10 dB, the values of $RIN_{TOT}$ and $RIN_{Laser}$ are essentially equal.

## 5.3 RIN measurement techniques

Different methods deal with the problem which is discussed earlier in this chapter. In subtraction method (Sec. 5.3.1), different noise sources are treated separately and subtracted from the total noise term. In the second method discussed in section 5.3.2, a special way of calibrating the system is introduced, while assuming that the thermal noise can be subtracted easily. This

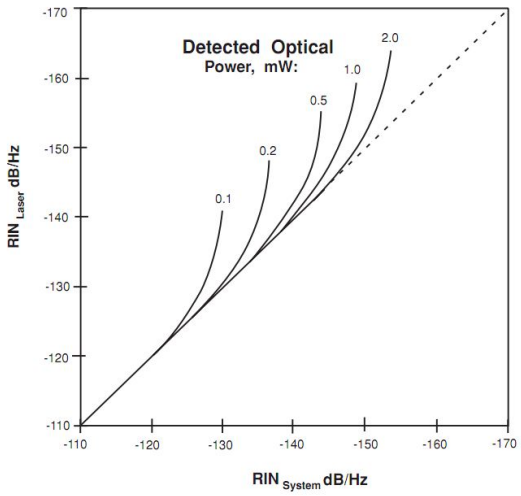


Figure 5.4: $RIN_{Laser}$ calculated from the measured $RIN_{System}(RIN_{TOT})$, versus average power [10]

method is widely used in fiber communications, where RIN measurement is done for modulated optical systems and a RIN value at a specific frequency is needed. Since the RIN value at only a particular frequency is of interest, the system is calibrated for the shot noise much more accurately. In the third method (Sec. 5.3.3), another technique for calibrating the system for the background noise in the system including shot noise is described. By utilizing a low-RIN reference laser, a high sensitive calibration system is achieved.

### 5.3.1 Subtraction method (Used in this project)

In this method, the extra noise sources are treated separately and subtracted from the total RIN. Thermal noise is measured by running the setup when the laser is turned off so there is no light on the photodetector. This term includes the dark photocurrent of the detector and the thermal noise sources of the electronics (total background noise). Shot noise, though, is calculated from the measured dc photocurrent when the laser is turned on. As it was mentioned in the explanation of the setup, our photodetector shows the dc average photocurrent using a bias monitor terminal. This terminal gives the voltage of the electrical signal. The photocurrent can be calculated by dividing this term by a constant factor of $1\,mV/\mu A$. Therefore, the shot noise power spectral density, which is white noise is calculated by

$$P_{n,shot} = (i_n)^2 \cdot 50\Omega = 2 \cdot q \cdot I_{dc} \cdot 50\Omega, \tag{5.7}$$

where $I_{dc}$ is the average photocurrent and $50\Omega$ accounts for the load resistance.

After these calculations, these noise terms are subtracted from the total measured RIN in linear units and then RIN in dB can be found. Great care must be taken when using this subtraction method to determine $RIN_{Laser}$. In subtracting small numbers from small numbers, errors in values that are close to the excess-noise value of the laser can have large effects. Errors in the amplitude accuracy of the frequency response of the diode can also cause exaggerated effects. It is important to know the frequency response for the total system before making noise subtractions [10].

#### Compensation for frequency dependent system parameters

Due to the fact that some of the system instruments do not have a flat frequency response over the entire spectrum, it is essential to compensate the result for these parameters. The frequency response of the photodetector, the microwave amplifiers, and the ESA have to be characterized, which is a difficult task. In this project, for compensating for the electrical gain unit, a normal $S_{21}$measurement is performed and the result is subtracted (in dB unit) from the spectrum obtained from the ESA.

### 5.3.2 Shot noise calibration method

The problem with the subtraction technique is that there is a need to determine several parameters of the system, such as the frequency response of the different components. The accuracy of such technique is rather limited due to the fact that one has to account for all of these parameters which is not an easy task. Also we must make sure that the impedance mismatch losses between the instruments are minimized or at least characterized very accurately [31]. However, in shot noise calibration method, there is a self-calibrating mechanism that takes care of these system parameters and makes the measurement results more accurate.

This technique is based on the fact that at a fixed bias current, various noise sources increase differently when decreasing the optical power by a variable optical attenuator (VOA). As it is illustrated in figure 5.5, thermal noise is not dependent on optical power, therefore by changing the power by a VOA, thermal noise does not change. On the other hand, shot noise increases linearly (10 dB/decade) and laser intensity noise term increases quadratically (20 dB/decade).

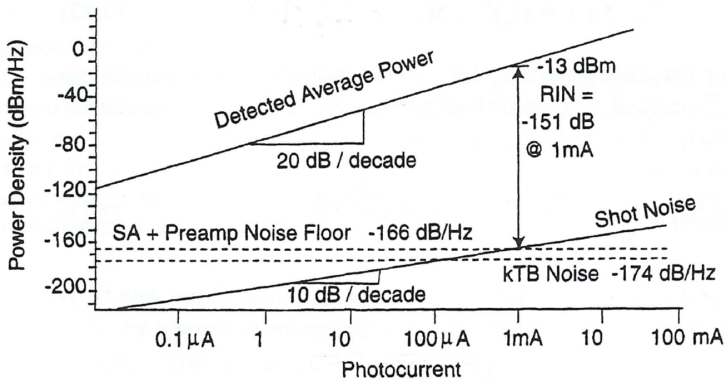


Figure 5.5: Variation of different noise terms by changing the photocurrent at a fixed bias current [25]

The total electrical noise as a function of detected photocurrent is [32]:

$$P_N = H(f) \cdot 10^{\frac{RIN}{10}} \cdot I_{dc}^2 + 2q \cdot H(f) \cdot I_{dc} + P_{th} \text{ [W/Hz]}, \tag{5.8}$$

where $P_N$ is total noise power spectral density (PSD) term on the ESA, $I_{dc}$ is the average dc photocurrent, $P_{th}$ accounts for the thermal noise term, and $H(f)$ is the trans-impedance of the system connecting the photodetector to the ESA. The first quadratic term of Eq. 5.8, corresponds to the quadratic relation between the intensity noise term and the total noise PSD. The second term is obtained from shot noise which is a linear relationship[1]. In this technique, a series of $P_N$ and $I_{dc}$ is measured at various settings of the optical attenuator ($\sim$ 10 points or more). Consequently, a second order curve such as shown in figure 5.6, will be obtained. In

[1]We imagine that shot noise can be calculated before the detection system, although we know that shot noise is generated in the electrical domain after the photodetection process

figure 5.6, the dashed line corresponds to the linear relationship of the shot noise only, when the intensity noise is negligible. At very low photocurrents, since the intensity noise is very small, the curve approaches the linear dashed line.

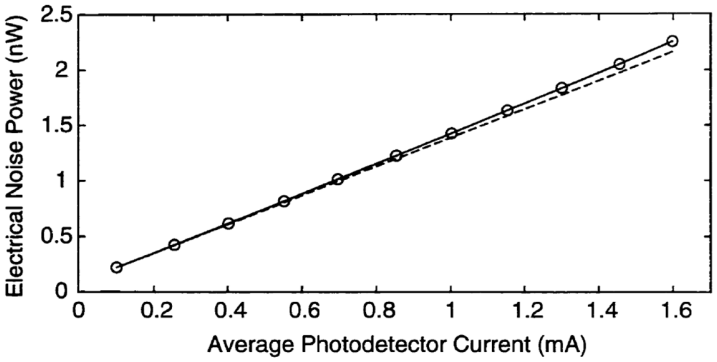


Figure 5.6: A series of measurement of $P_N$ and $I_{dc}$ at various settings of the VOA [32]

By doing a least squares fit of a quadratic function ($Y = a_1 \cdot X^2 + a_2 \cdot X + a_3$) to the measured data, the coefficients of such equation can be extracted. By assuming such general equation for the corresponding equation of 5.8, the system calibration term ($H(f)$) and subsequently $RIN$ is found by the following relations:

$$H(f) = \frac{a_2}{2q}, \tag{5.9}$$

$$RIN = 10 \cdot log(\frac{a_1}{H(f)}). \tag{5.10}$$

This fitting must be done for each frequency of interest. For example, if 801 frequency points are defined to cover a spectrum of 20 GHz, this fitting process is applied for each of the frequency points. However, all these 801 fittings can perhaps be done with a simple coding simultaneously.

The advantages of this method are that it has lower uncertainty (higher accuracy), and it benefits from a self-calibrating approach. On the other hand, it has some limitations as well. Clearly, the measurement procedure is rather long, but most importantly, this method can only be applied to shot-noise limited systems. For instance, it is not suitable for our detection system, because the detection system used in this project is thermally-limited , i.e. even at highest received optical power, our system is limited by thermal noise. In order to have a shot noise limited system, one should have lasers with much higher output power, or electronics with much lower noise figure (NF).

### 5.3.3 Low-RIN laser calibration method

This method is very similar to the second method, shot noise calibration technique. The similarity is that it benefits from the same concept, nonetheless the trans-impedance of the detection system $H(f)$ is found in a simpler way. The need for measuring a series of different photocurrents points in the previous method, makes the procedure quite long. Hence, a low-RIN laser can be used in this method in order to calibrate the detection system. Utilizing such a low-RIN laser means that in equation 5.8, the first term is negligible. Assuming that the thermal noise can be managed separately when there is no light on the photodetector, the remaining parts of the equation will be:

$$P_N = 2q \cdot H(f) \cdot I_{dc} \text{ [W/Hz]}, \tag{5.11}$$

Therefore, the calibration is only done once by running the setup only at one photocurrent point instead of a series of points. The use of the low-RIN laser is as a reference device only to find $H(f)$ in a shot noise limited system. Thus after running the setup with the reference device, the device under test (DUT) can be characterized. As an example in [33], a solid state laser with an electronic loop controlling the current of the pumping diode in order to reduce the intensity noise, has been utilized as the reference laser. Such device has a negligible RIN for frequencies higher than the relaxation oscillation frequency. Next, the device under test replaces the reference laser and its RIN value is calculated through Eq. 5.8.

Operation of this calibration method is also based on assuming that the system is shot-noise limited, therefore it is not applicable for our detection system, which is thermally limited. Furthermore, the other limitation was that there were no available low-RIN lasers at the wavelength of our DUT laser. The lasers used in this project, were VCSELs emitting at 850 nm, however the wavelength of our low-RIN DFB lasers were at 1550 nm, meaning that they could not be used as the reference.

In [34] and [35], a definition for system calibration factor is specified, in which an idea similar to what has been stated here is incorporated. It is claimed that by using this technique, measurement uncertainty levels below 0.4 dB can be achieved and laser RINs more than 10 dB below shot RIN can be assessed if suitable optical isolation (>60 dB) is used.

#### 5.3.3.1 Low-RIN lasers

For characterization of the reference laser, the important point is that the relative intensity noise contribution can be neglected in comparison with the shot noise term. In order to evaluate such a property of a laser, it is convenient to normalize the measured PSD by the detected photocurrent. According to the equation 5.8, the normalized PSD (i.e. $PSD_{dut}$ divided by $I$) is independent of photocurrent only if the RIN term can be neglected. This property can be used to test a laser whether it can be used as a reference laser. For such a reference source, for the shot noise measurement, the normalized PSD becomes independent of the optical power. In practice, the reference measurement is done only once at a high photocurrent [33].

Very-low-RIN lasers are used to determine the noise figure of optical-fiber amplifiers, which are essential for building faster and more-efficient optical communications systems. Demand for better techniques to calibrate the response and sensitivity of a RIN-measurement system is also increasing with the appearance of commercial distributed-feedback (DFB) lasers and diode-pumped Nd:YAG lasers exhibiting very low RIN [36].

### 5.3.4 Correction factor

It should be mentioned that it is necessary to add a +2 dB correction factor to all noise measurements. Due to the nature of noise, an under-response of 2 dB happens, when noise is assumed as input signal of superheterodyne spectrum analyzers. The details of why such a correction factor is needed can be found in Appendix A.

However, in many electrical spectrum analyzers, there is often a noise marker function, which automatically accounts for this correction factor. By turning the noise marker function on, the instrument will set the following settings automatically. It reads out the average noise level (average detector is chosen). It adds +2 dB correction factor. It also computes the mean value of the 32 display points around the marker. It finally normalizes the value to a 1–Hz noise power bandwidth.

If this feature is not available in the spectrum analyzer, the insertion of +2 dB correction factor and also normalization to 1–Hz noise bandwidth (often favorable in noise measurements) should be done manually .

# 6 Results

In the experimental work of this project, the subtraction method, explained in section 5.3.1 was chosen based on the experimental setup illustrated in Fig. 5.1. The reason to choose this method was that our detection system was thermally limited. Therefore, neither of the second or the third technique is applicable to our system. Furthermore, there was no available low-RIN laser emitting at 850 nm at our lab facilities, to be used as the reference laser, needed for the third technique.

The aim of the work is to measure the RIN diagrams of the second generation high-speed VCSELs and verify whether they meet the requirements of future fiber optics communication standards which are based on such VCSELs at 850 nm as transmitter in the links. These high-speed VCSELs can be incorporated in short reach links in different standards such as Fibre Channel, Infiniband, and Ethernet. Before realizing the measurements, it was expected that these high-speed VCSELs should meet the requirements of the upcoming standards quite well, due to their optimized design of the structure.

## 6.1 Practical issues of the measurements

The detection system that was mounted based on the available instruments and components, was thermally limited. There are a number of issues that were considered in the RIN measurements in this project.

**Sensitivity** The first major difficulty of the RIN measurement is to have a sufficient sensitivity, to be able to detect the low noise levels on the ESA. Microwave amplifiers with low NF and high gain are needed for increasing the sensitivity. The sensitivity can be enhanced even further, by cascading two amplifiers, given that the first one has a particularly low-NF and the second one a high-gain.

**Compensation for the amplifier** As it was described before, accurate compensation for the frequency dependent system parameters is needed in subtraction method. Hence, an $S_{21}$ measurement was carried out for the detection system, from the output of the photodetector, to the input of the ESA. Thereafter, this factor was subtracted (in dB) from the result obtained by the ESA to compensate for the gain and the frequency response of the microwave amplifiers.

**ESA settings** A couple of parameters should be set on the ESA, in order to get more accurate results. In the table 6.1, the ESA settings in this project are listed.

| Span | RBW | VBW | Input attenuator | Noise marker function | Sweep points |
|---|---|---|---|---|---|
| 0–20 GHz | 30 KHz | 30 KHz | 0 dB | ON | 801 |

Table 6.1: ESA setting

The resolution bandwidth (RBW) of the ESA should be set as low as possible, to give the highest precision and also the best sensitivity [25]. In [37], the explanation about how RBW relates to the sensitivity of the ESA can be found. In practice, it was observed that RIN values are dependent on RBW setting. If it is set to a high value, ESA will give higher RIN values. It

is also essential to use a consistent RBW for all measurements because of the higher uncertainty if different RBWs are used. Thus, 30 KHz was chosen for RBW which gives a reasonable short sweep time.

Video bandwidth (VBW) does not really matter since smoothing of the data can be done by post-processing of measured data. A value that gives a short sweep time was chosen.

Moreover, there is an internal attenuator at the input of spectrum analyzers. In the case of measuring noise, setting this attenuator to zero attenuation results in the best instrument sensitivity [25].

Finally, the noise marker function should be activated. This function has several features, such as assigning a +2 dB correction factor that should be inserted in all noise measurements. (See Appendix A for details)

**Coupling of a multi-mode laser** RIN measurement of single-transverse-mode lasers is simpler compared to multi-transverse-mode lasers. The big problem faces when one is looking for RIN in multi-mode lasers. VCSELs are inherently single-longitudinal-mode, while they can have multiple modes in the transverse direction. In fact, the high-speed VCSELs in this project have multiple modes; the wider the oxide aperture, the more transverse modes are emitted from the VCSEL.

In multi-transverse-mode VCSELs, the different modes compete for the gain in active region. Since they have different divergence, they will couple to the fiber differently if the fiber/VCSEL alignment is not perfect. It is shown that if our system has a mode-selective coupling, then higher RIN values for $f < 2GHz$ are obtained. This is avoided if the alignment is optimized so that the coupling efficiency is the same for all of the modes [20]. This excessive noise due to mode-competition is called mode-partitioning noise (MPN). One might also observe multiple-resonance peaks in the RIN spectrum if the transmission link contains mode-selective losses or mode-selective coupling to optical fiber [20, 38].

The core of multi-mode fibers are very thin with a diameter of either 50 $\mu$m or 62.5 $\mu$m (in our case 50 $\mu$m). Therefore, the alignment of the fiber tip to get the highest fiber coupling efficiency is a very difficult task. For this reason, it is necessary to test whether all of the modes are coupled into the fiber and that they reach the photodetector with same proportion. In this alignment process, the other end of the fiber is connected to an optical power meter. We should align the fiber tip until the highest possible optical power is measured. A coupling efficiency of typically >60% can be reached.

In practice, aligning the fiber to get the highest power into the fiber does not guarantee that the partitioning of the modes is also equal. Consequently, extra fine-tuning to get the minimum RIN values (especially at low frequencies) needs to be done after doing the alignment for the highest power. Clearly, the second fine tuning is more difficult and takes much trial-and-error.

Not only the fiber tip should be aligned very precisely, but also the fiber itself should be fixed somehow. We can assume that there are many modes in different locations of the cross-section of the core of the fiber. Thus by bending or moving the fiber to some extent, the transverse location of the modes may vary. Furthermore, some of the highest order modes may leak out of the core of the fiber to the cladding if their divergence is very large.

**Reflections** The third major issue in almost all of the optical measurements is the unwanted effect of back reflections. Some of the output light from the VCSEL can get reflected back to the laser structure from different facets. These reflections can be from the lenses, the tip of the fiber, any bending in the fiber itself, or even from the surface of the detector. The influence of reflections on RIN is mentioned in Section 3.5. The fiber alignment or moving the fiber can also result in different reflection mechanism, meaning that the influence of reflection in RIN diagrams is not static. Some other fine tuning or moving the fiber might be needed to get a RIN diagram which is less influenced by the reflections. Since the effect of reflections in RIN is periodical, the

effect is easily observed. Some fine tuning should be done until we can get rid of the periodical fluctuations in the RIN diagram.

It was actually observed that touching and moving the optical fiber as well as the VOA can change the reflection of light and the coupling efficiency, which shows a clear effect on the RIN diagram. Also it helps if the length between the tip of the fiber and where it starts to bend, to be sufficiently long.

**How to get nice plots** A nice plot means that first, the noise levels are greater than the sensitivity of the measurement system. Secondly, reflections are sufficiently low so that no periodic fluctuations exist in the curves. Thirdly, mode-partitioning noise is suppressed by a very precise fiber alignment. For this purpose, the fiber alignment is first done for getting the highest possible optical power to the detector using an optical power meter. Then we connect the ESA and perform some fine-tuning in order to get rid of the effects of reflections. Thereafter, the fiber should be fixed and not touched anymore, otherwise effects of reflections will appear again.

An extensive amount of time and energy in this project was spent on how to get an optimized coupling of these different modes into the multi-mode fiber with same proportion and at the same time avoid any possible reflection effects.

**Our problematic ESA** Unfortunately, our ESA had a problem with its local oscillator calibration. As it is shown in the figure 6.1, at the beginning the instrument was giving false values at two frequency regions. However, during the time of the project, the calibration system of the instrument improved itself and the problem was less and only at one region. For solving this problem, the false regions were removed and numerical values were estimated by interpolation using MATLAB. After I removed the false data, I used Savitzky-Golay FIR smoothing filter to smooth-out the signal. Then the extrapolation was carried out. The method used for the extrapolation in MATLAB was smoothing-spline which seemed to give better results compared to other methods to preserve the outline or the shape of the measured plots.

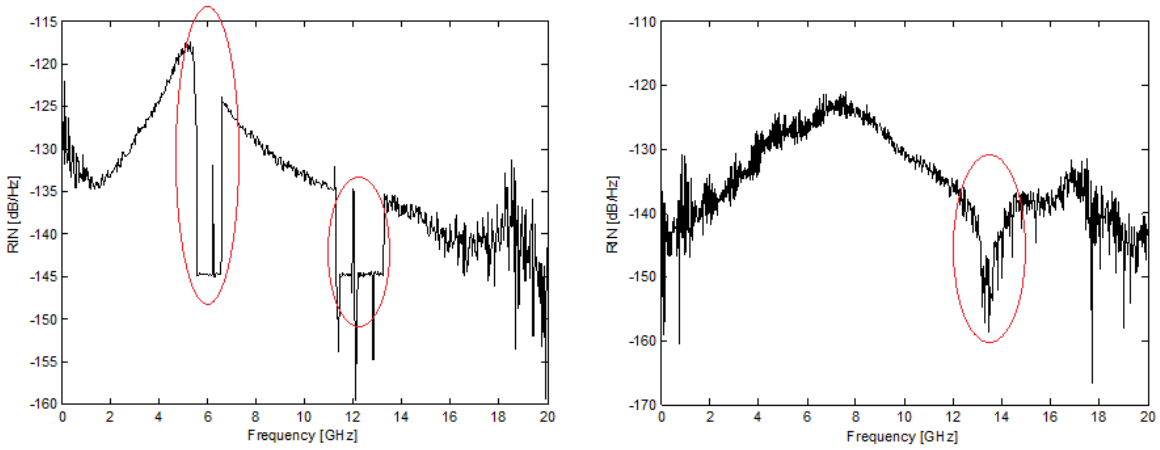


Figure 6.1: Our problematic ESA, early in the project (Left) and later in the project (Right), showing false data at certain regions.

## 6.2 VCSELs chip

In this project, VCSELs with four different oxide aperture diameters were investigated and compared to see if they qualify for the new standards in terms of intensity noise (RIN).

In figure 6.2, part of the chip containing VCSELs in an array of $8 \times 14$ is depicted. Each row comprises VCSELs with equal oxide aperture diameters. In this project, VCSELs from column-7 and row-1 to row-4 were chosen, having oxide apertures of $7\,\mu m$, $9\,\mu m$, $11\,\mu m$, and $13\,\mu m$.


Figure 6.2: Microscope image of the chip 10B8- Gen II high speed VCSELs

As it was previously mentioned, RIN depends on the bias current, therefore these VCSELs are characterized at different bias currents starting form 1 mA (if it is higher than its threshold) to thermal roll-over current in a step of 1 mA.

It should be noted that obtaining nice plots for high bias currents is a difficult task. The reason is that by increasing the bias current, the RIN diagrams become more damped. Therefore, the required sensitivity for detecting that noise level becomes higher. Furthermore, since at higher output power there is a risk of damaging the photodetector, it is essential to use a variable optical attenuator (VOA) before the detector to attenuate the optical power. Thus every time the bias current is increased, the attenuation should be increased to protect the detector; this makes it more challenging to detect the low power noise by the electrical spectrum analyzer. For instance, RIN diagram for VCSEL 0107 with $7\,\mu m$ oxide aperture at room temperature (RT), is illustrated only up to 4 mA, although the thermal roll-over for this VCSEL occurs at 8 mA; but the quality of the RIN diagrams for bias currents more than 4 mA were poor and severely limited by the noise limit of the detection system.

## 6.3 RIN diagrams of the VCSELs

In table 6.2, the current (electrical) versus power (optical) characteristics of the VCSELs are shown. In VCSELs with wider oxide aperture, the optical (photon) density is lower, therefore the threshold current is larger. For the measurements at $85°C$ ambient temperature, the device performance is slightly degraded, thus it has a higher threshold current and weaker optical power. Typically at higher temperatures, the optical gain of the laser is decreased. However, in order to reduce the temperature sensitivity of these high-speed VCSELs, the cavity resonance is placed at the long wavelength part of the gain spectrum to compensate for the temperature induced

reduction of gain with improved mode/gain overlap. Therefore, by increasing the temperature, at first the threshold current starts to decrease, but then it increases again [2]. The maximum output powers at 85°$C$ operation were not measured, but the maximum current $I_{max}$ shows that the thermal roll-over occurs at lower currents.

| VCSEL size [$\mu m$] | 7 ($RT$) | 9 ($RT$) | 11 ($RT$) | 13 ($RT$) | 7 (85°$C$) | 9 (85°$C$) | 11 (85°$C$) | 13 (85°$C$) |
|---|---|---|---|---|---|---|---|---|
| $I_{th}$ [mA] | 0.23 | 0.50 | 0.71 | 1.1 | 0.4 | 0.7 | 1.3 | 2.3 |
| $I_{max}$ [mA] | 8.3 | 12.5 | 16.4 | 22.7 | 5.6 | 8.5 | 10.7 | 14.7 |
| $P_{max}$ [mW] | 4 | 7.6 | 11 | 15.5 | – | – | – | – |

Table 6.2: IPV characteristics of the VCSELs

### 6.3.1 VCSELs with $7\,\mu m$ oxide aperture

The RIN values are shown for the VCSEL with the smallest oxide aperture, VCSEL 0107, at room temperature in figure 6.3 and at 85°$C$ in figure 6.4. Based on the optical measurement data which is shown in table 6.2, measurements were done at bias currents starting from 1 mA to thermal roll-over which is at 8 mA. However, since the plots for the bias currents higher than 4 mA did not have enough quality, only the results for 1 mA to 4 mA are plotted. As it can be seen in the figure for 85°$C$ operation, the noise levels are higher, and the resonance frequencies are slightly shifted to lower frequencies.

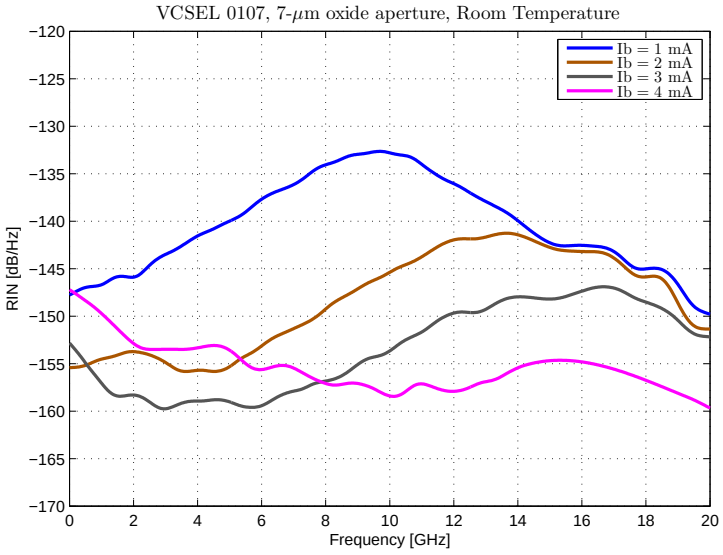


Figure 6.3: RIN values for VCSEL with $7\mu m$ oxide aperture diameter at room temperature operation

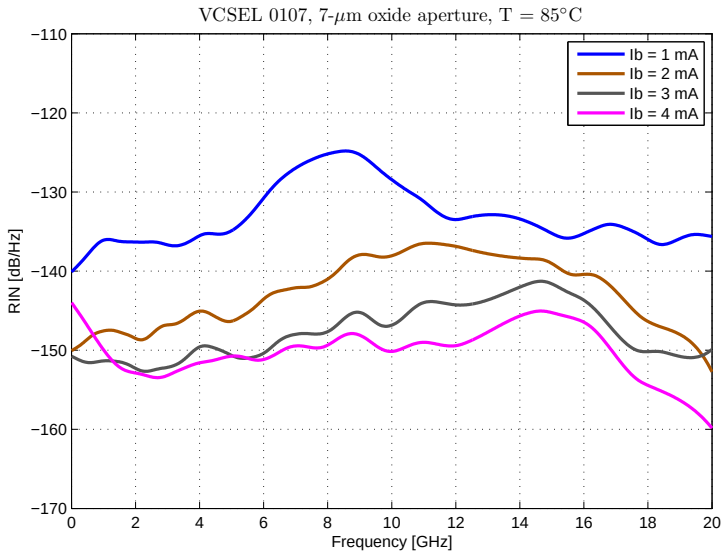


Figure 6.4: RIN values for VCSEL with $7\mu m$ oxide aperture diameter at $85°C$ operation

### 6.3.2 VCSELs with $9\,\mu m$ oxide aperture

The RIN values are shown for the VCSEL 0207 with $9\,\mu m$ oxide aperture, at room temperature in figure 6.5 and at $85°C$ in figure 6.6.

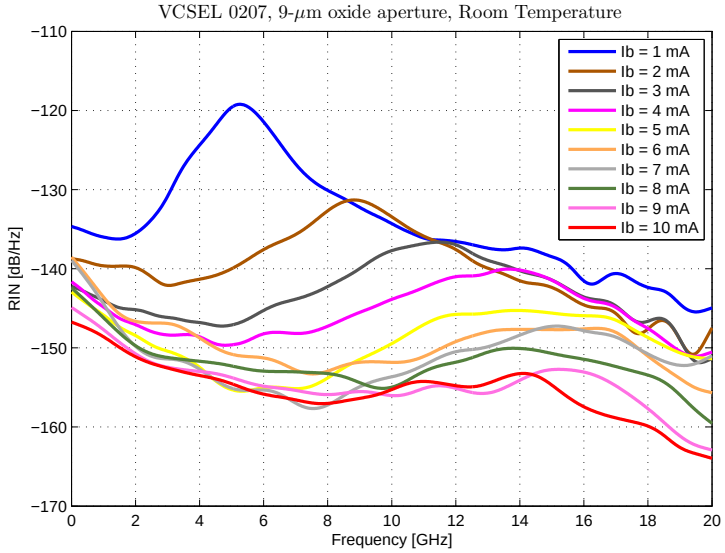


Figure 6.5: RIN values for VCSEL with $9\mu m$ oxide aperture diameter at room temperature operation

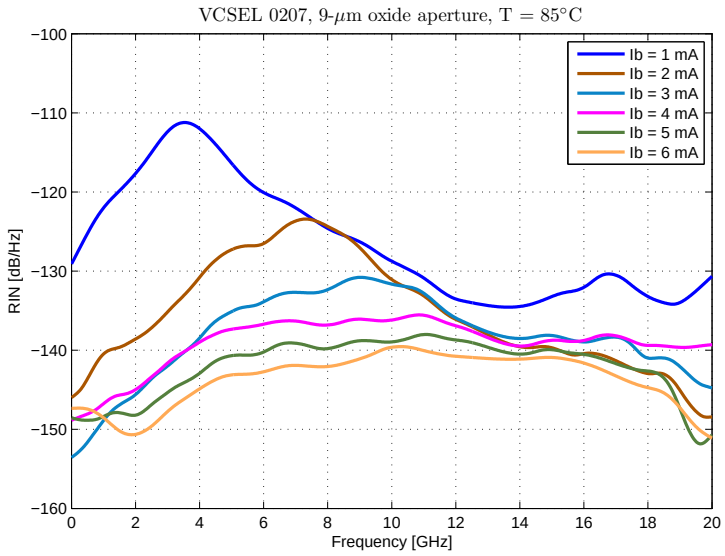


Figure 6.6: RIN values for VCSEL with $9\mu m$ oxide aperture diameter at $85°C$ operation

### 6.3.3 VCSELs with $11\,\mu m$ oxide aperture

Figure 6.7 and 6.8 show the RIN values for the VCSEL 0307 with $11\,\mu m$ oxide aperture, at room temperature and at $85°C$, respectively. The rise in the values at low frequencies is unfortunately due to mode-partitioning noise (MPN). MPN exists in multi-mode lasers when there is a mode-selective coupling of the laser light into the fiber.

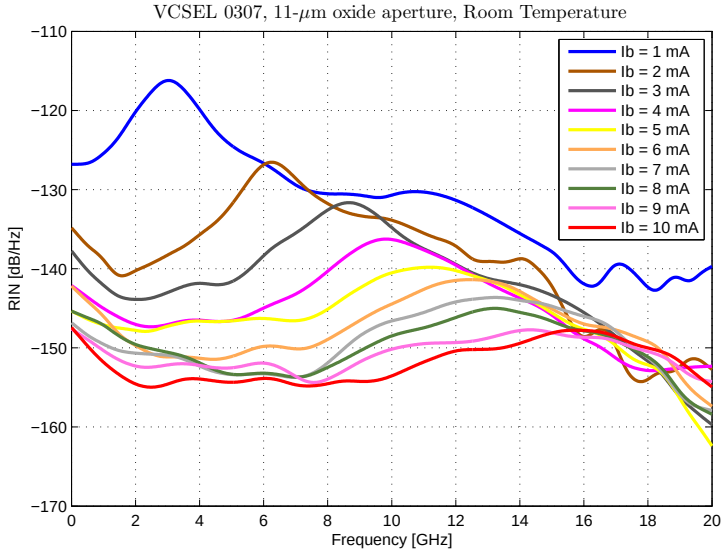


Figure 6.7: RIN values for VCSEL with $11\mu m$ oxide aperture diameter at room temperature operation

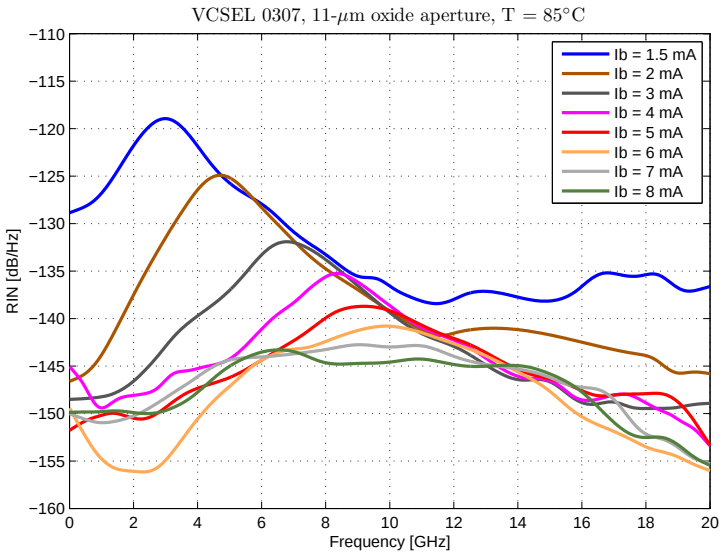


Figure 6.8: RIN values for VCSEL with $11\mu m$ oxide aperture diameter at $85°C$ operation

### 6.3.4 VCSELs with $13\,\mu m$ oxide aperture

Finally, the RIN values are illustrated in figure 6.9 and 6.10, for the VCSEL 0407 with $13\,\mu m$ oxide aperture , at room temperature and at $85°C$, respectively. For the $85°C$ temperature measurement, VCSEL 0407 was accidentally burned by mistake, therefore VCSEL 0406 was used instead. These two lasers have the same oxide aperture diameters and should have very similar properties.

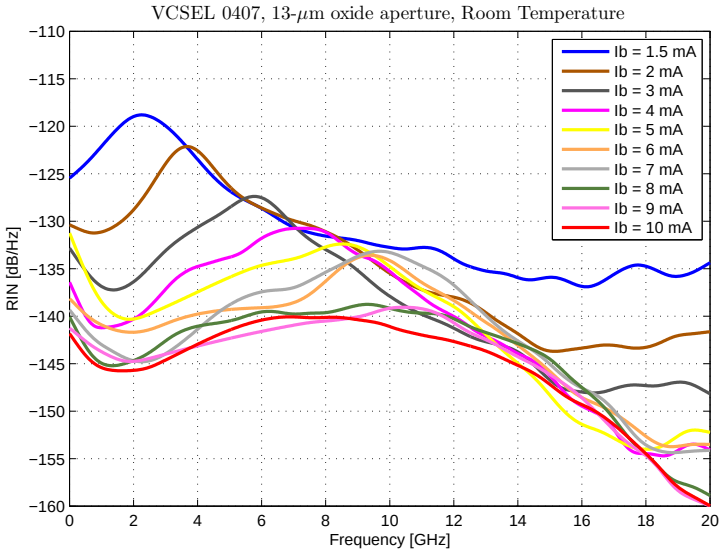


Figure 6.9: RIN values for VCSEL with $13\mu m$ oxide aperture diameter at room temperature operation

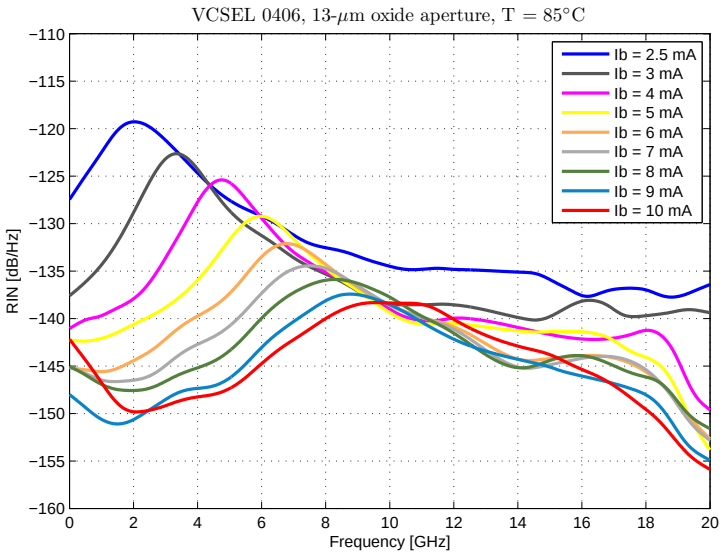


Figure 6.10: RIN values for VCSEL with $13\mu m$ oxide aperture diameter at $85°C$ operation

## 6.4 Maximum RIN values as a function of the size of the oxide aperture

It was already mentioned that the maximum value for intensity noise of lasers is around the resonance frequency for each bias current. In the diagrams illustrated in figure 6.11 and 6.12, these maximum values are shown as a function of the size of the oxide aperture at RT and $85°C$. By looking at these diagrams we can conclude that VCSELs with larger oxide aperture have higher RIN. The reason to have higher RIN values when the oxide aperture is wider is that the optical (photon) density $S_b$ is lower, since the optical volume ($V_p$) is larger. As it was discussed in Section 2.3.2, the equations obtained from the small-signal analysis of the VCSEL show that the resonance frequency ($f_r$) and the damping factor ($\gamma$) of a VCSEL depend on optical density. As the photon density is increased (by increasing the injection current or due to narrower oxide aperture), the resonance frequency increases as $f_r \propto \sqrt{S_b}$. On the other hand, since $\gamma \propto f_r^2 \propto S_b$, the damping increases at a faster pace. Evidently, higher resonance frequencies and larger damping factors generally lead to reduced RIN values in RIN spectrum.

Moreover, at higher temperatures the RIN values are higher and the resonance frequencies are lower compared to the ones at lower temperature, as expected.

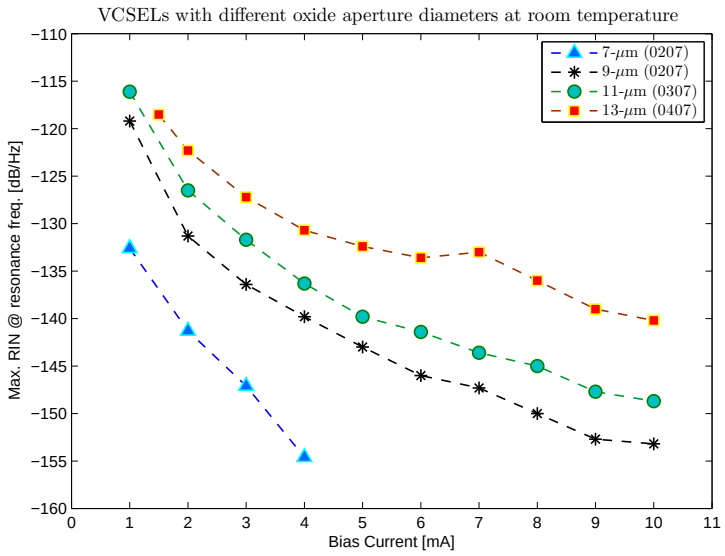


Figure 6.11: Comparison of maximum RIN value for VCSELs with different oxide aperture sizes at room temperature operation

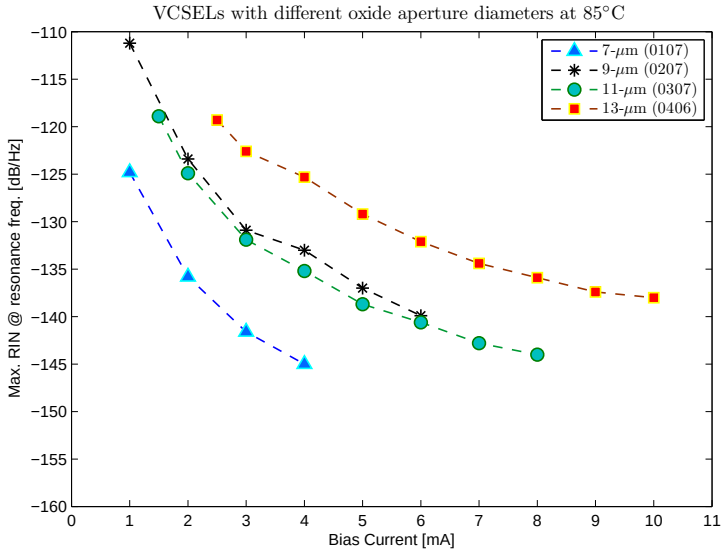


Figure 6.12: Comparison of maximum RIN value for VCSELs with different oxide aperture sizes at 85°$C$ operation

## 6.5 RIN requirement in different standards

VCSELs have attractive features that have made them the most popular transmitter choice in short range optical communication links. For short reach local area network (LAN) environments, including optical networks in data centers [storage area networks (SANs)] and high performance computing (HPC) systems, VCSELs have already, to a great extent, replaced other lasers. Fibre Channel (FC), Gigabit Ethernet (GbE), and Infiniband are among the most important standards in short range communications [39]. The links in these standards are based on high-bandwidth

multi-mode fiber (e.g., OM3 fiber) at wavelength of 850 nm. It is interesting to investigate whether these high-speed VCSELs can satisfy the requirements that have been specified in these various protocols in terms of intensity noise performance.

In the case of Fibre Channel standard, the first product (1GFC with 1 Gbps data rate) was available at market in 1997. A summary of different products of this standard is shown in table 6.3 [40, 41]. Obviously, the criteria specified for RIN has become more and more stringent during the evolution of this protocol.

| Product Naming | Market availability | VCSEL RIN |
|---|---|---|
| 1GFC | 1997 | -116 dB/Hz |
| 2GFC | 2001 | -117 dB/Hz |
| 4GFC | 2005 | -118 dB/Hz |
| 8GFC | 2008 | -128 dB/Hz |
| 16GFC | 2011 | -128 dB/Hz |
| 32GFC | 2014 | -130 dB/Hz |

Table 6.3: RIN specifications in different Fibre Channel products, for 32GFC the value is mentioned in RIN(OMA) definition [40, 41]

By looking at table 6.3, a jump in RIN specification is evident. The reason is that since 8GFC standard, a new link budget spreadsheet model (*IEEE 10G*) has been used, in which the accuracy of the model is enhanced [40, 42].

In HPC systems, the newest value specified for RIN is $-128\,dB/Hz$ [41]. Moreover, in 10 Gigabit Ethernet protocol, the standard at 850 nm is called 10GBASE-SR. In this standard, the demand for the RIN value is $-128\,dB/Hz$. Since RIN values always depend on the transmitter properties, thus some conditions are also set. These conditions are that the minimum extinction ratio ($ER_{min}$) should be $3\,dB$ and the minimum average transmitter power ($P_{avg,tx,min}$) of $-7.3\,dBm$ is required [43].

In some standards, a new definition called RIN(OMA) is introduced instead of giving a specification for RIN. For instance, in table 6.3, 32GFC standard, in contrast to older products, has defined that RIN(OMA) should be below $-130\,dB/Hz$ instead of RIN. Furthermore, in IEEE802 Serial PMD standard at 850 nm, the specification is also based on RIN(OMA) definition, which has to be below $-125\,dB/Hz$, while the minimum optical modulation amplitude (OMA) should be $357\,\mu W$ [44].

Based on these values that are mentioned in different standards, we can estimate that a RIN value of less than about $-130\,dB/Hz$ would satisfy the demands in most cases. If we consider the measured data in the Figs. 6.11 and 6.12, the RIN values for low bias currents are higher than $-130\,dB/Hz$. However, we need only to consider the RIN values at certain bias currents since these VCSELs are usually biased at several mA in order to achieve sufficient modulation bandwidth. Therefore, if we look at the measured RIN values for bias currents around 6 to 8 mA, they are fortunately lower than the demands for maximum acceptable RIN value.

### 6.5.1 RIN(OMA) definition

In the definition of RIN, one can say that it assumes that the laser is fully modulated (maximum extinction ratio[1]). However, there is a desire to operate the laser at a reduced modulation amplitude due to some advantages. First of all, the optical modulation amplitude (OMA) needs to be defined. OMA is the difference between the power levels at high and low state levels in

[1] In telecommunication, extinction ratio is the ratio of the optical power level when the laser is ON, or "1" state, divided by the optical power level when the laser is OFF or the "0" state [15].

the digital modulation. The fully modulated laser (maximum OMA) and the reduced OMA are illustrated in Fig. 6.13. Reduction of OMA gives some features such as better eye quality in high speed optical transmitters, lower chirp, reduced turn-on delay due to the fact that the laser is not off at "0" state, among others. The Fibre Channel standard is also written specifically to permit lasers to be operated at reduced OMA.

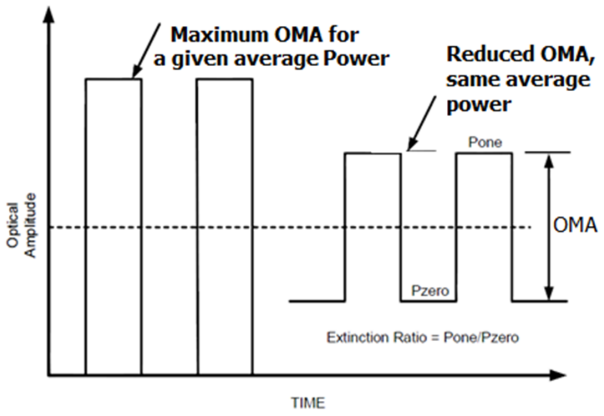


Figure 6.13: Maximum OMA and reduced OMA have the same average power but different power levels at high and low states [44].

In Eq. 4.5, the formula for calculating the power penalty, induced from RIN, was given as a function of the quality factor (BER) for a given amount of intensity noise ratio. However, it should be noticed that this formula is based on assuming that the laser is operating at maximum OMA. RIN is a parameter which is dependent on the OMA. If the laser operates at a lower OMA, the laser must have a lower RIN value in order to obtain the same BER, e.g. $BER < 10^{-12}$.

Consequently, due to this dependency of the required RIN value on the OMA value at which the laser is operating, a new definition so-called RIN(OMA) is provided as [27]

$$RIN(OMA) = 10 \cdot log\left(\frac{P_n}{P_m \cdot \Delta f}\right) \tag{6.1}$$

where $RIN(OMA)$ is the relative intensity noise referred to optical modulation amplitude (OMA), $P_n$ is the electrical noise power when the laser modulation is OFF, and $P_m$ is the electrical signal power when the laser modulation is ON. This expression shows that by attempting to reduce the extinction ratio of the laser by decreasing the modulation, the value of $P_m$ will decrease proportionally resulting in a higher value of $RIN(OMA)$.

As it was discussed before, this new definition is being used in the new products of the Fibre Channel standards as well as some other new standards. However, this definition has one more criteria wherefore it is called $RIN_{12}(OMA)$. The 12 subscript denotes that in the setup which is proposed for RIN measurement, in addition to have modulation to change the OMA, there has to be a certain amount of existing reflection . Based on this definition, a 12 dB back reflection from a single reflective plane must exist in order to ensure that the transmitter RIN is being characterized under a more stressful, but realistic link condition [27].

Finally, the setup for measuring $RIN_{12}(OMA)$ is proposed as it is depicted in Fig. 6.14. Note the existence of the 12-dB reflection in this setup.

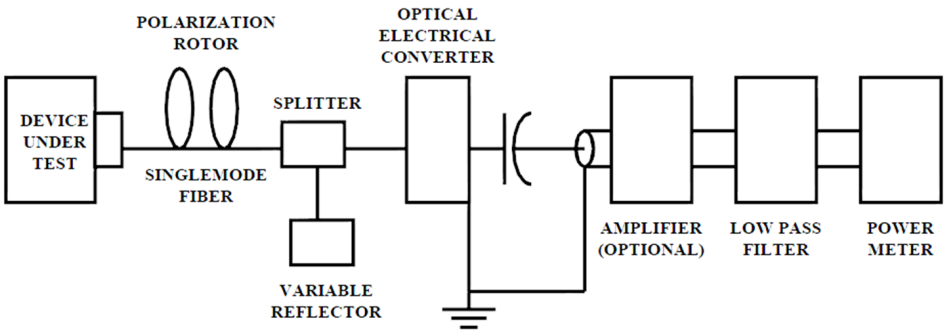


Figure 6.14: Setup for measuring $RIN_{12}(OMA)$ [44]

# 7 Extracting intrinsic dynamic VCSEL parameters from RIN measurements

After the experimental work of the project, the analysis part was performed. In the preceding sections, RIN spectra were measured in order to evaluate the VCSELs whether they satisfy the demands in different fiber optics communication standards. However, RIN measurement has another interesting application, in which the high speed modulation performance of the device can be characterized. RIN transfer function was introduced in Section 3.6 in analogy with small signal modulation ($S_{21}$)[1] transfer function in Section 2.3.2.

Conventionally, in order to evaluate the high speed modulation performance of a device, typical small-signal modulation response ($S_{21}$) experiments are carried out. Intrinsic dynamic laser parameters ($f_r$, $\gamma$, and $f_p$) can be extracted from fitting the measured data with a small-signal transfer function (Eq. 2.10), specified for the high-speed VCSELs. However, these parameters ($f_r$ and $\gamma$) can also be extracted from RIN measurements.

In this chapter, the conventional method of $S_{21}$ tests are described and the measured data is provided. Then the fitting procedures to extract the intrinsic dynamic parameters is carried out for $S_{21}$ diagrams, as well as RIN diagrams.

## 7.1 *D*- and *K*-factor from $S_{21}$-measurements

Fig. 7.1 illustrates the schematic of the setup used for measuring the small-signal modulation response. The critical tool used for this experiment was an *Agilent N5230A* PNA-L network analyzer.

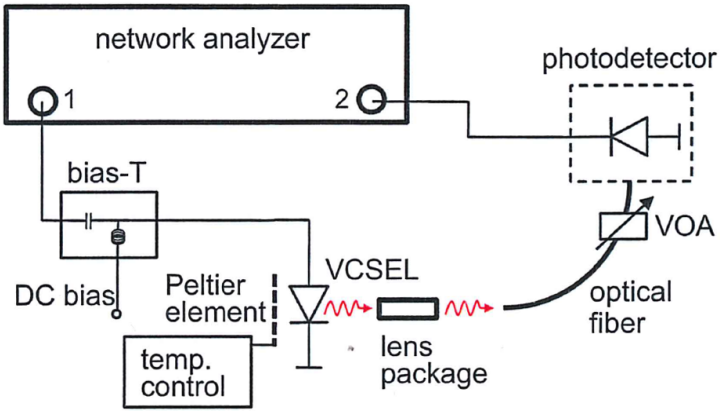


Figure 7.1: Schematic illustration of the experimental setup for measuring the small signal modulation response ($|S_{21}|$) [2]

After performing a through calibration procedure to remove the effects of the microwave cables and the bias-T, the VCSEL is mounted. A bias-T is needed to add the d.c. bias to the a.c. signal from the port-1 of the network analyzer. The output photocurrent is connected to the port-2

[1] An element of the Scattering Matrix related to the forward voltage gain of a 2-port network

of the network analyzer. The network analyzer is set to show the magnitude of $S_{21}$ in dB unit versus frequency. The measured data should therefore be fitted to the magnitude of Eq. 2.10.

$$H(f) = A \cdot \left| \frac{f_r^2}{f_r^2 - f^2 + j\frac{f}{2\pi}\gamma} \cdot \frac{1}{1 + j\frac{f}{f_p}} \right|^2 \tag{7.1}$$

where A is an amplitude factor accounting for the slope efficiency of the laser, the dynamic response of the photodetector, and the insertion loss of the microwave probe [2]. Consequently, this formula can be written in dB unit as :

$$|H(f)| = 10 \cdot log(C \frac{f_r^2}{(f_r^2 - f^2)^2 + (\frac{\gamma}{2\pi})^2 f^2} \frac{1}{(1 + j(\frac{f}{f_p})^2)}) \tag{7.2}$$

Eq. 7.2 is used in the fitting process in order to extract the following parameters: $f_r$, $\gamma$, and $f_p$.

However, some compensations and considerations for the measured data should be done before performing the fittings. The high speed GSG RF probe and the photodetector do not have a flat frequency response over the entire 20 GHz bandwidth. Thereby, their frequency response should be compensated and subtracted (in dB) from the $S_{21}$ curves in order to obtain more precise values. Moreover, it is better if the VOA is set to a certain attenuation value from the beginning, so that there would be no need to change it for higher bias currents.

After fitting these parameters, they can be related to the $K$- and $D$- factors, which are the quality indicators of the modulation performance of the device. These two factors were already discussed in Section 2.3.2. In order to find the $D$-factor, we simply plot $f_r$ versus $\sqrt{I_b - I_{th}}$ for the fitted values. The slope of this figure at low bias currents gives the $D$-factor (Eq. 2.11). Similarly, the $K$-factor is obtained from plotting $\gamma$ versus $f_r^2$. The slope of this plot gives the $K$-factor (Eq. 2.12).

## 7.2 *D*- and *K*-factor from RIN measurements

The RIN transfer function (in linear unit) was mentioned in Eq. 3.3 in Section 3.6. The RIN plots from the measurements in Section 6.3 can be fitted to this equation, and thereby the intrinsic parameters of the device can be extracted.

It should be noted that the RIN transfer function in Eq. 3.3 is not in dB/Hz unit. Therefore, the equation that should be fitted to the measurement is:

$$RIN[\text{dB/Hz}] = 10 \cdot log(\frac{Af^2 + B}{(f_r^2 - f^2)^2 + (\frac{\gamma}{2\pi})^2 f^2}) - 10 \cdot log(\Delta f) \tag{7.3}$$

In a similar manner to the $S_{21}$ case, the $D$- and $K$-factor parameters are calculated from the extracted $f_r$ and $\gamma$ coefficients.

## 7.3 Comparison between two techniques

As already mentioned, $S_{21}$ measurements are typically used for the extraction of intrinsic modulation parameters. However, as it is evident from the $S_{21}$ transfer function in Eq. 2.10, the modulation response can be limited by the parasitic capacitance of the device ($f_p$) which reduces the accuracy in determining $\gamma$ and $f_r$. In this case, RIN measurements would probably offer better results since there is no influence from the electrical parasitics.

However, there is a disadvantage that exists when dealing with RIN diagrams. Obtaining high-quality curves is in general a difficult task compared to $S_{21}$ plots because we have to work with very low level signals which requires a more sensitive detection system.

## 7.4 Fitting results

In this section, the fitted plots are shown. In each subsection, the fittings for RIN and $S_{21}$ as well as the extracted $D$- and $K$- factors from these two techniques are illustrated for each VCSEL at a specific temperature.

### 7.4.1 $7\,\mu m$ oxide aperture at RT

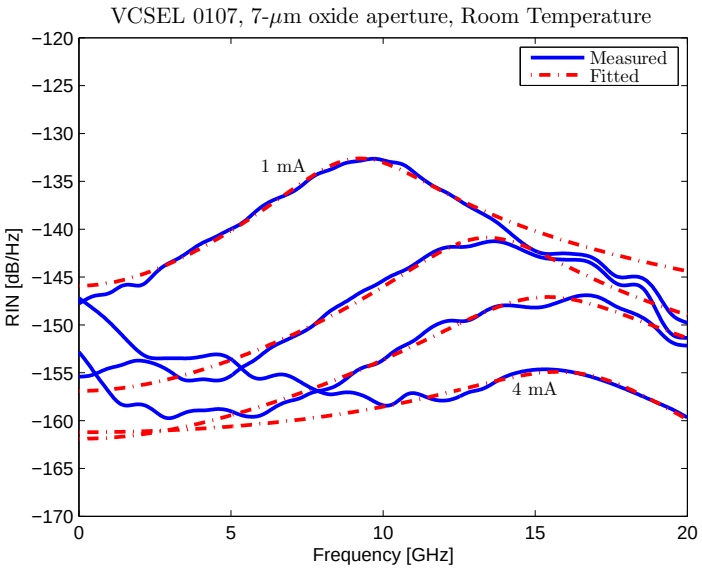


Figure 7.2: Fitting of RIN transfer function, for VCSEL with $7\mu m$ oxide aperture diameter at room temperature operation.

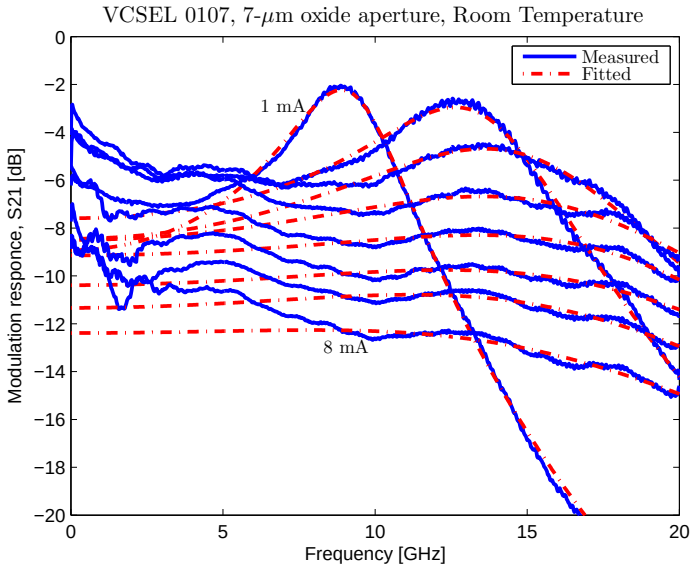


Figure 7.3: Fitting of modulation transfer function for small-signal modulation response, for VCSEL with $7\mu m$ oxide aperture diameter at room temperature operation.

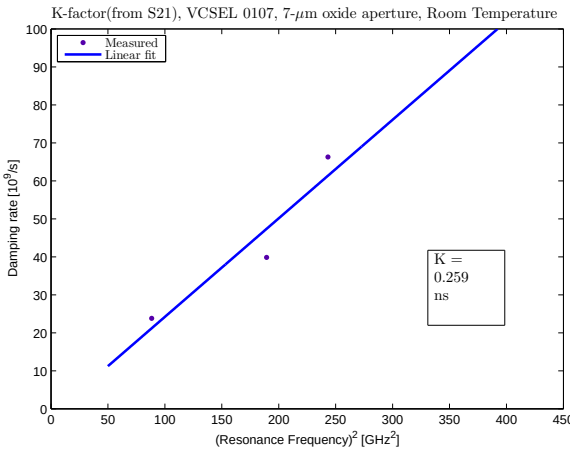


(a) K-factor from $S_{21}$

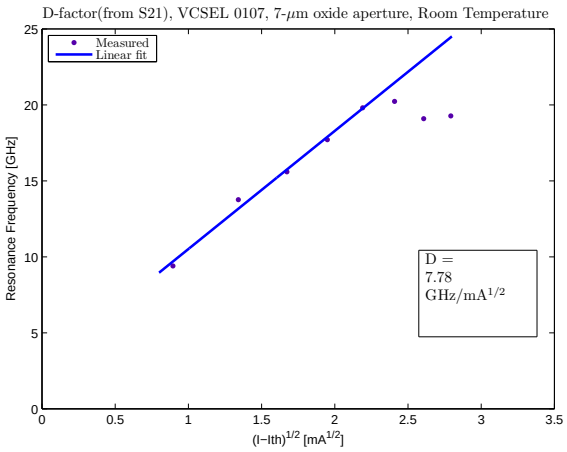


(b) D-factor from $S_{21}$

Figure 7.4: Extracted parameters from $S_{21}$measurement, for VCSEL with $7\mu m$ oxide aperture diameter at room temperature operation.

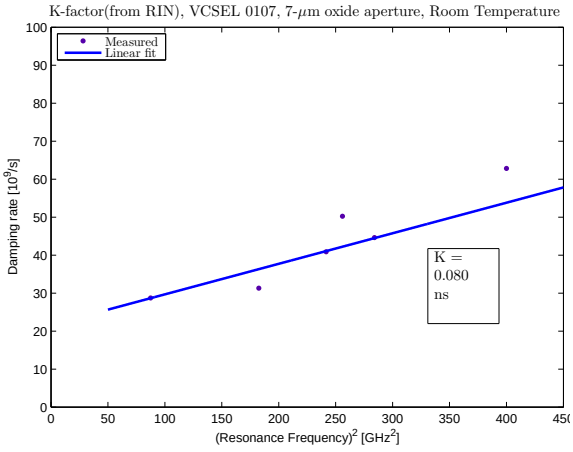


(a) K-factor from $RIN$

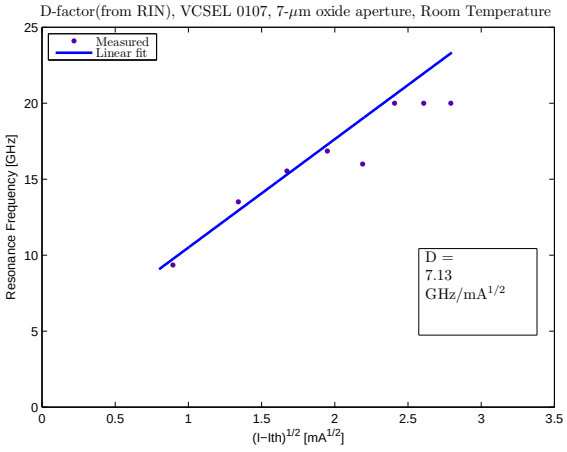


(b) D-factor from $RIN$

Figure 7.5: Extracted parameters from $RIN$ measurement, for VCSEL with $7\mu m$ oxide aperture diameter at room temperature operation.

### 7.4.2 $9\,\mu m$ oxide aperture at RT

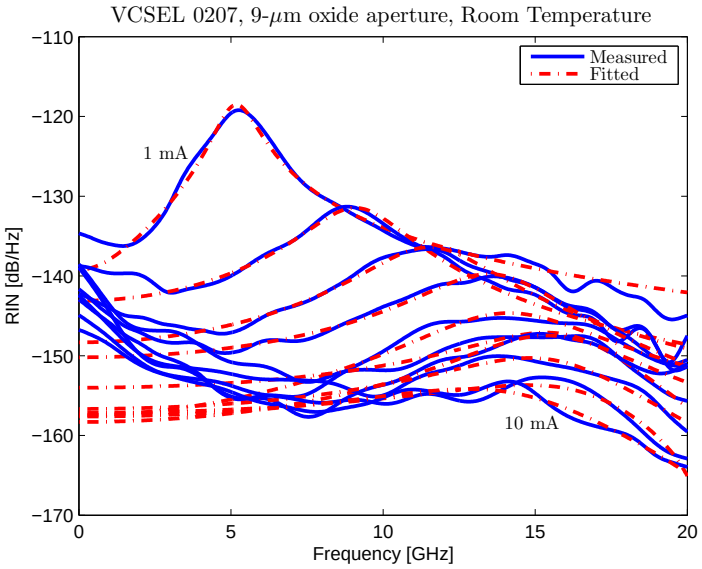


Figure 7.6: Fitting of RIN transfer function, for VCSEL with $9\mu m$ oxide aperture diameter at room temperature operation.

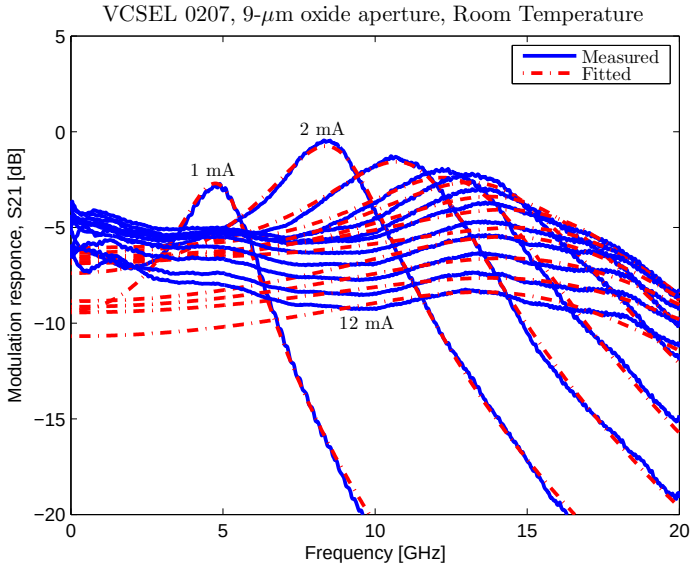


Figure 7.7: Fitting of modulation transfer function for small-signal modulation response, for VCSEL with $9\mu m$ oxide aperture diameter at room temperature operation.

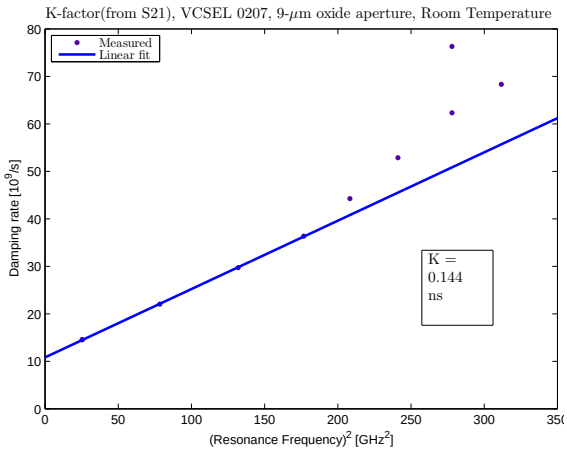


(a) K-factor from $S_{21}$

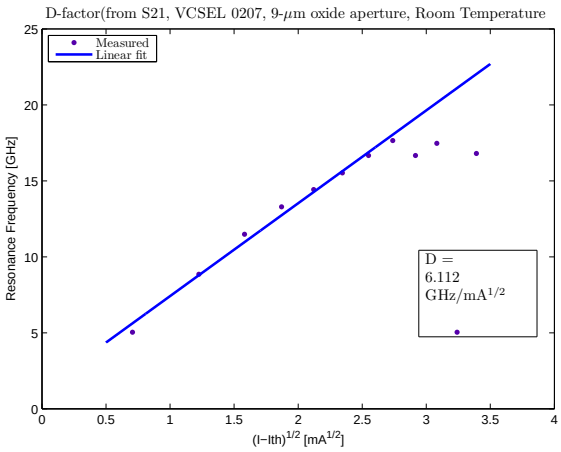


(b) D-factor from $S_{21}$

Figure 7.8: Extracted parameters from $S_{21}$measurement, for VCSEL with $9\mu m$ oxide aperture diameter at room temperature operation.

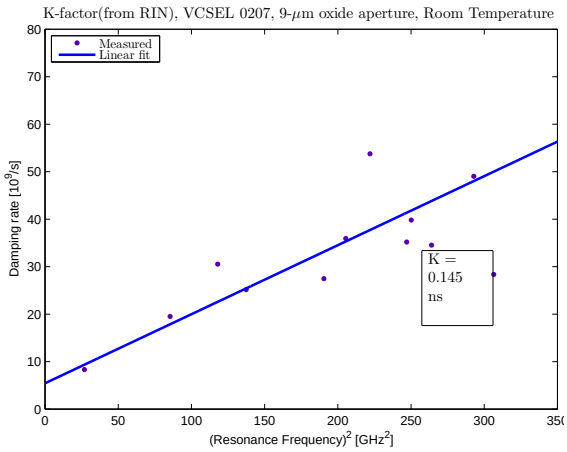


(a) K-factor from $RIN$

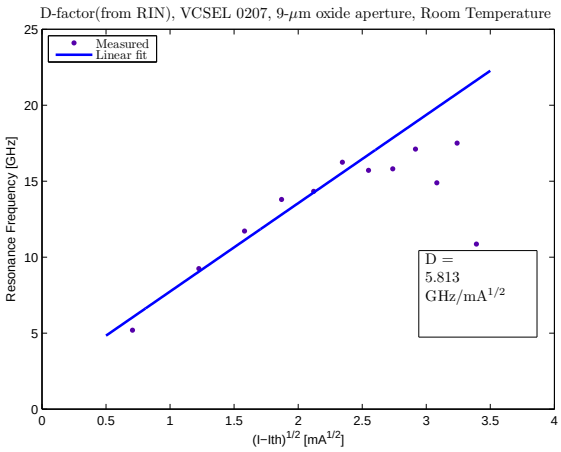


(b) D-factor from $RIN$

Figure 7.9: Extracted parameters from $RIN$ measurement, for VCSEL with $9\mu m$ oxide aperture diameter at room temperature operation.

### 7.4.3 11 $\mu m$ oxide aperture at RT

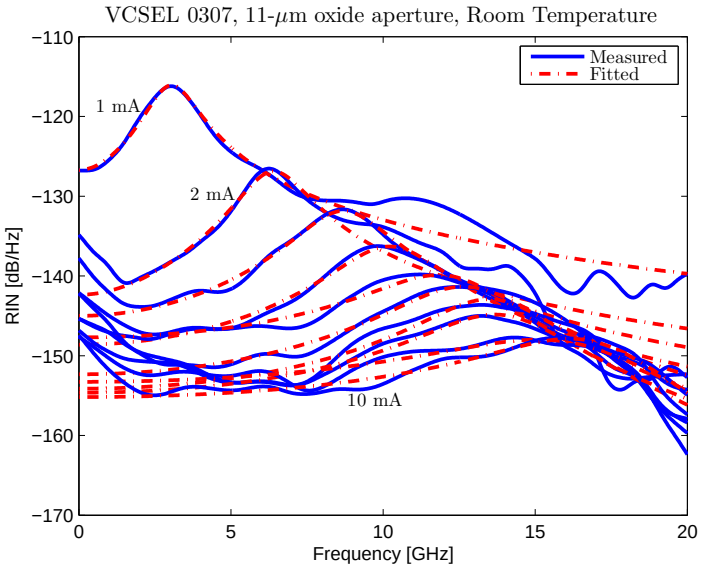


Figure 7.10: Fitting of RIN transfer function, for VCSEL with 11$\mu m$ oxide aperture diameter at room temperature operation.

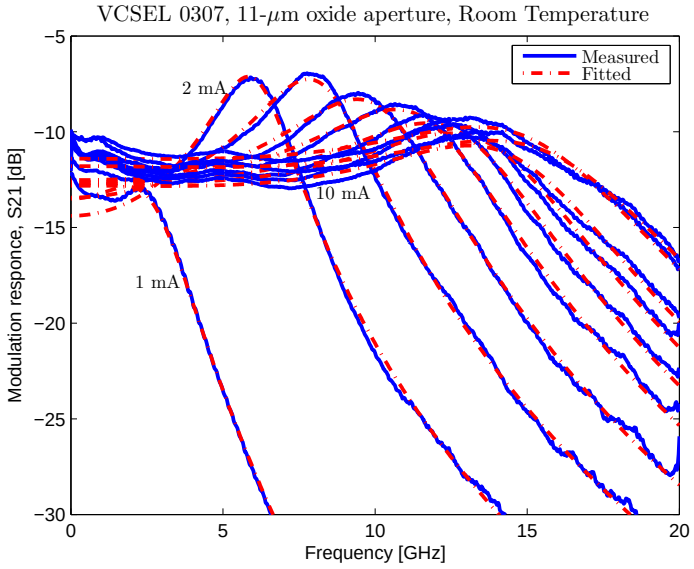


Figure 7.11: Fitting Fitting of modulation transfer function for small-signal modulation response, for VCSEL with 11$\mu m$ oxide aperture diameter at room temperature operation.

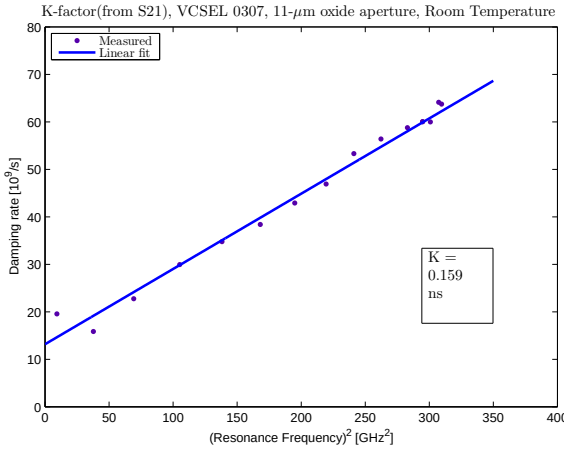


(a) K-factor from $S_{21}$

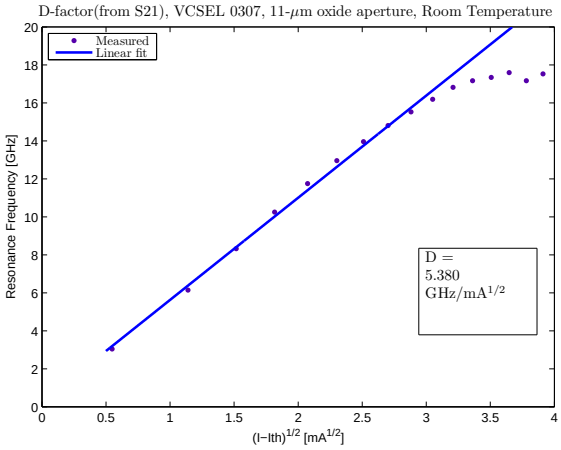


(b) D-factor from $S_{21}$

Figure 7.12: Extracted parameters from $S_{21}$measurement, for VCSEL with $11\mu m$ oxide aperture diameter at room temperature operation.

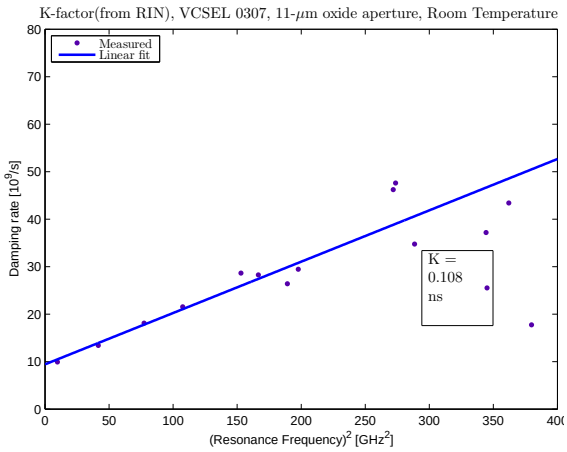


(a) K-factor from $RIN$

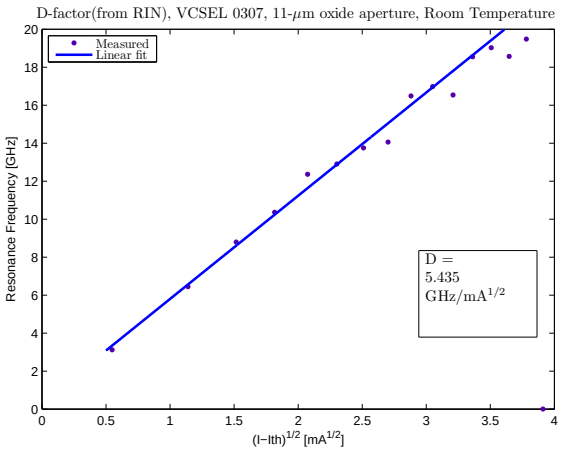


(b) D-factor from $RIN$

Figure 7.13: Extracted parameters from $RIN$ measurement, for VCSEL with $11\mu m$ oxide aperture diameter at room temperature operation.

### 7.4.4 $13\,\mu m$ oxide aperture at RT

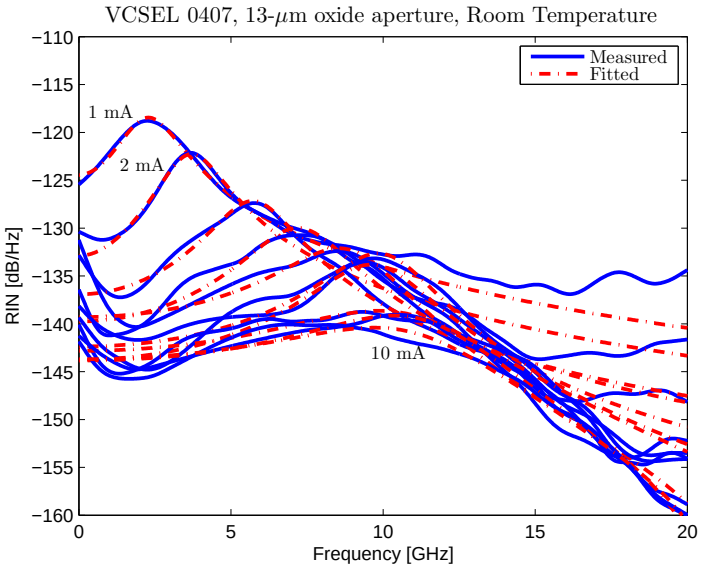


Figure 7.14: Fitting of RIN transfer function, for VCSEL with $13\mu m$ oxide aperture diameter at room temperature operation.

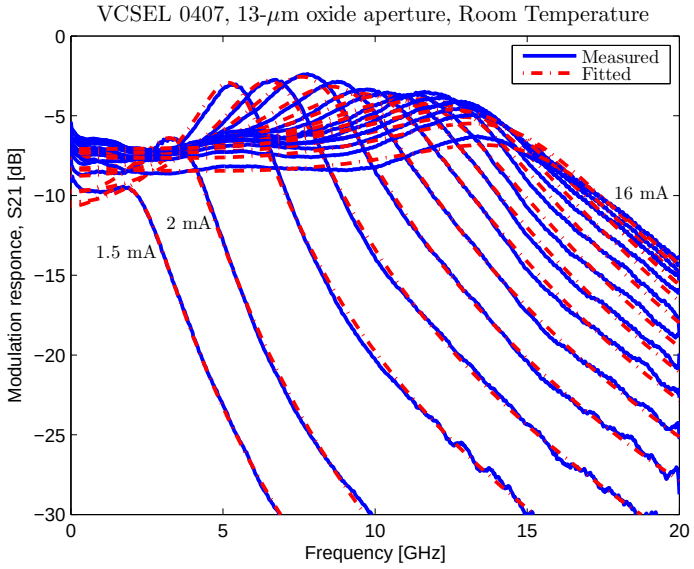


Figure 7.15: Fitting of modulation transfer function for small-signal modulation response, for VCSEL with $13\mu m$ oxide aperture diameter at room temperature operation.

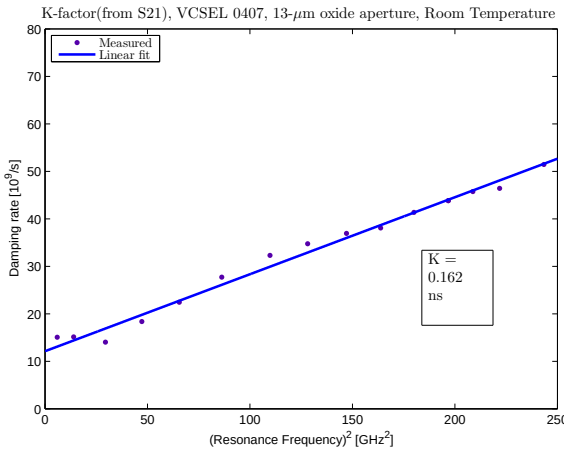


(a) K-factor from $S_{21}$

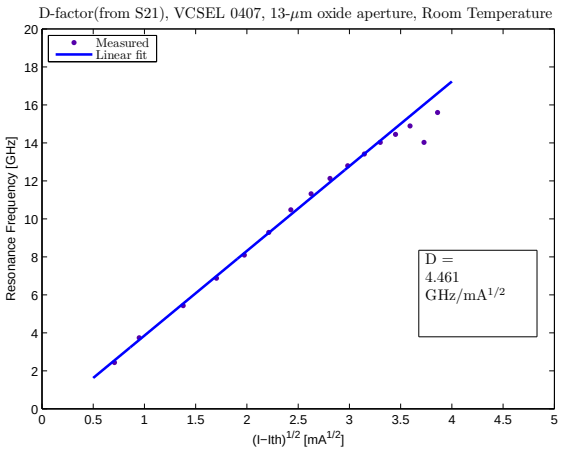


(b) D-factor from $S_{21}$

Figure 7.16: Extracted parameters from $S_{21}$measurement, for VCSEL with 13$\mu m$ oxide aperture diameter at room temperature operation.

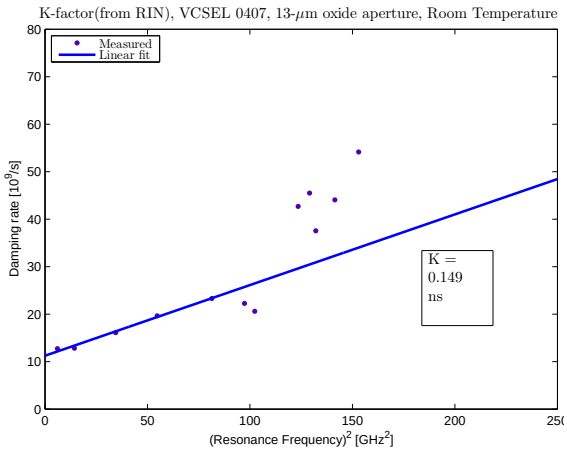


(a) K-factor from $RIN$

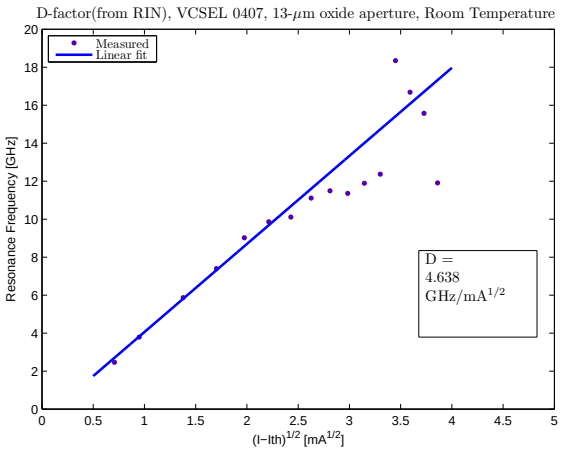


(b) D-factor from $RIN$

Figure 7.17: Extracted parameters from $RIN$ measurement, for VCSEL with 13$\mu m$ oxide aperture diameter at room temperature operation.

### 7.4.5 $7\,\mu m$ oxide aperture at $85°C$

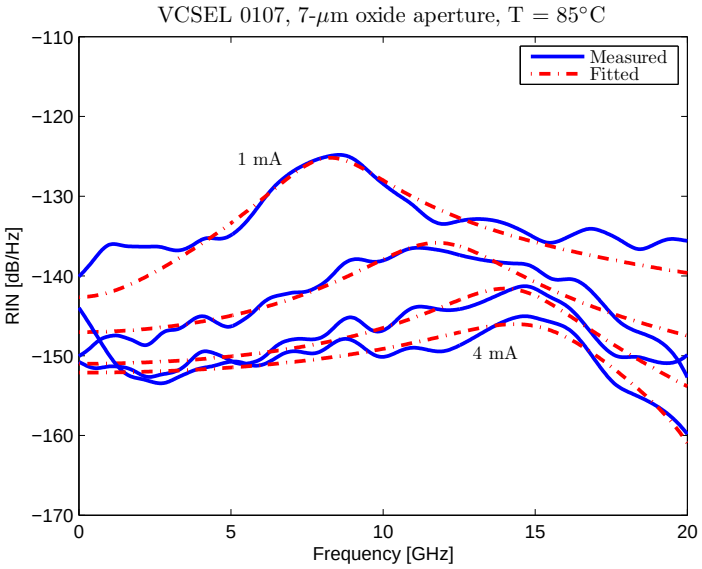


Figure 7.18: Fitting of RIN transfer function, for VCSEL with $7\mu m$ oxide aperture diameter at$85°C$ operation.

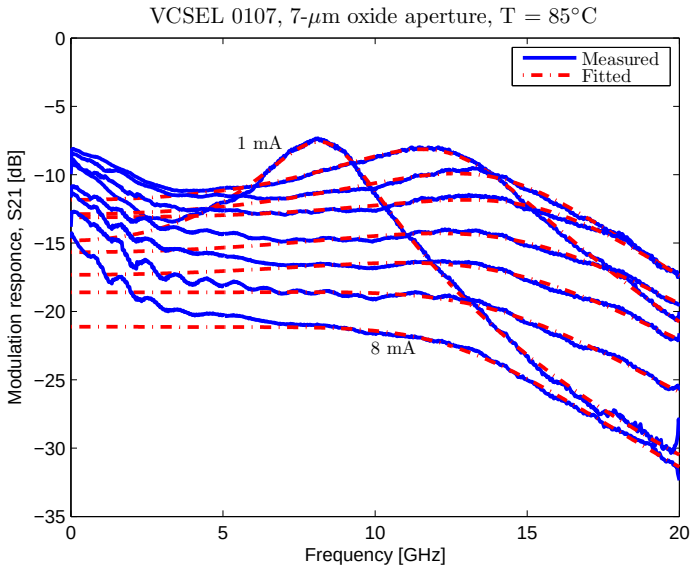


Figure 7.19: Fitting of modulation transfer function for small-signal modulation response, for VCSEL with $7\mu m$ oxide aperture diameter at$85°C$ operation.

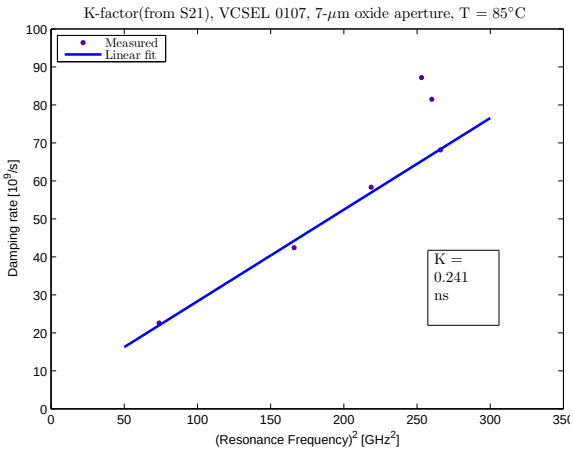


(a) K-factor from $S_{21}$

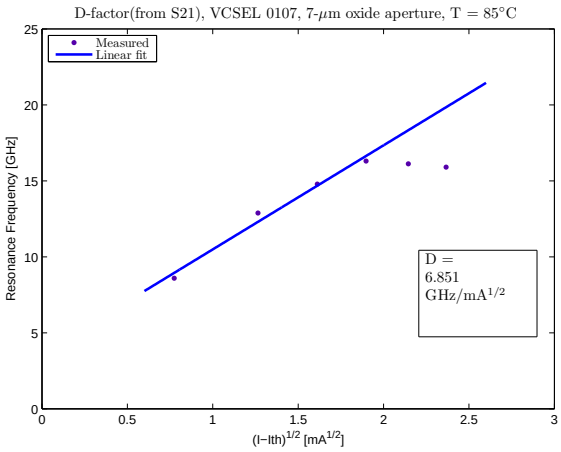


(b) D-factor from $S_{21}$

Figure 7.20: Extracted parameters from $S_{21}$measurement, for VCSEL with $7\mu m$ oxide aperture diameter at$85°C$ operation.

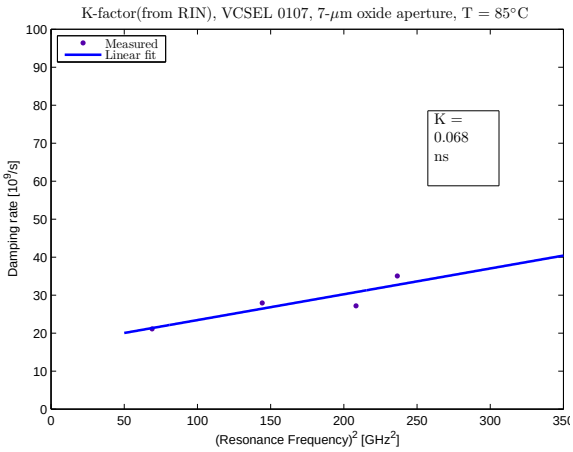


(a) K-factor from $RIN$

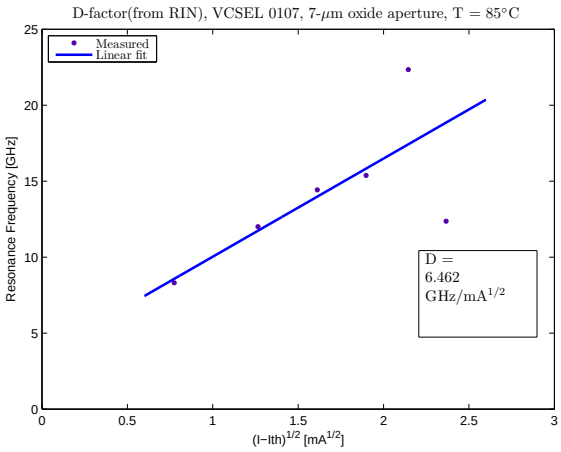


(b) D-factor from $RIN$

Figure 7.21: Extracted parameters from $RIN$ measurement, for VCSEL with $7\mu m$ oxide aperture diameter at$85°C$ operation.

### 7.4.6 $9\,\mu m$ oxide aperture at $85°C$

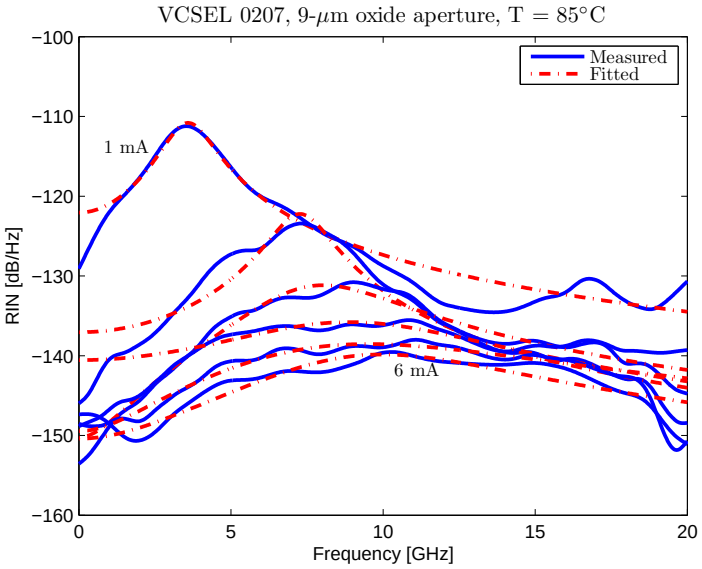


Figure 7.22: Fitting of RIN transfer function, for VCSEL with $9\mu m$ oxide aperture diameter at$85°C$ operation.

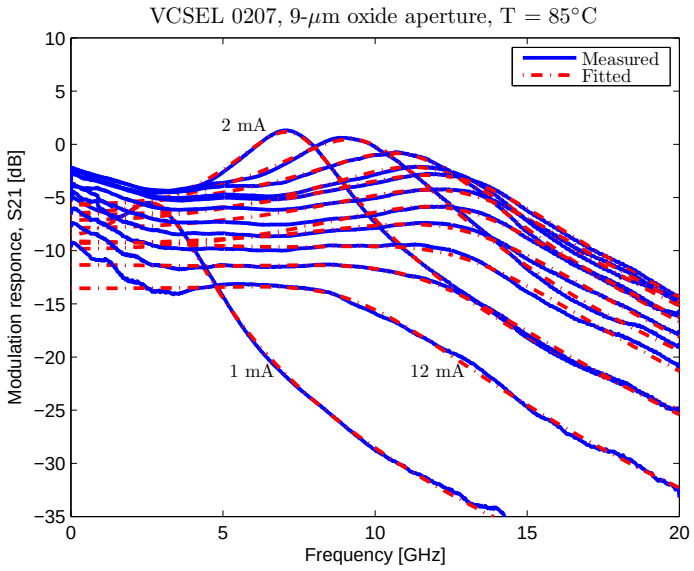


Figure 7.23: Fitting of modulation transfer function for small-signal modulation response for VCSEL with $9\mu m$ oxide aperture diameter at$85°C$ operation.

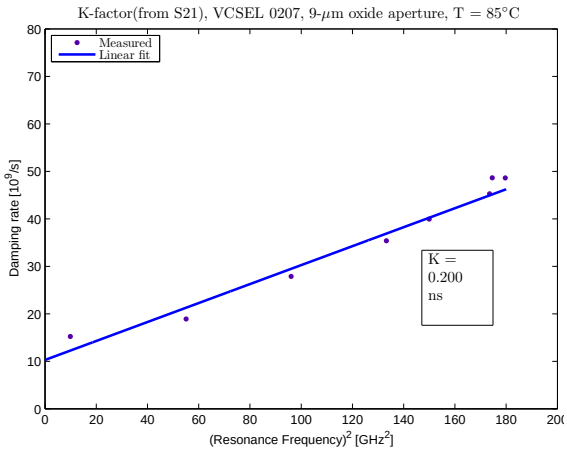


(a) K-factor from $S_{21}$

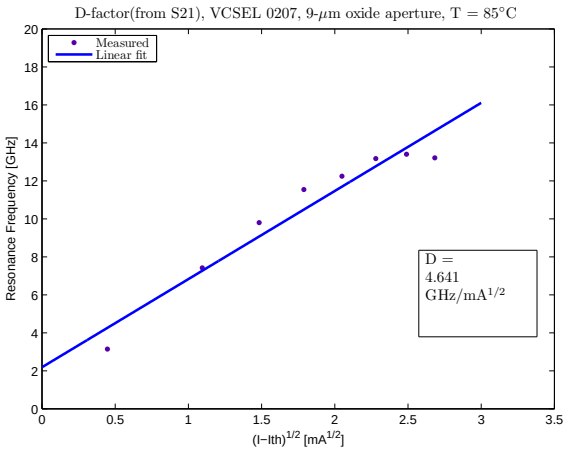


(b) D-factor from $S_{21}$

Figure 7.24: Extracted parameters from $S_{21}$measurement, for VCSEL with $9\mu m$ oxide aperture diameter at$85°C$ operation.

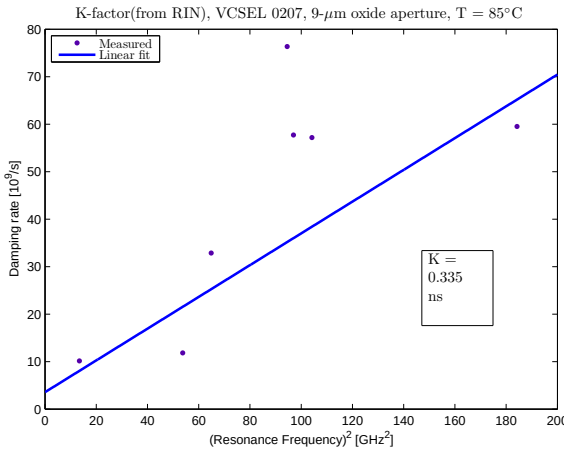


(a) K-factor from $RIN$

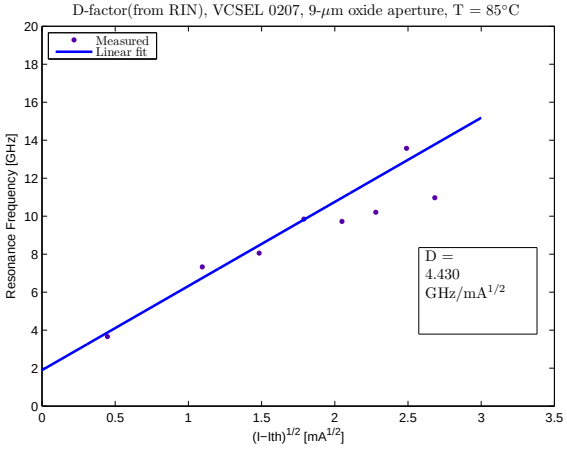


(b) D-factor from $RIN$

Figure 7.25: Extracted parameters from $RIN$ measurement, for VCSEL with $9\mu m$ oxide aperture diameter at$85°C$ operation.

### 7.4.7 11 $\mu m$ oxide aperture at 85°$C$

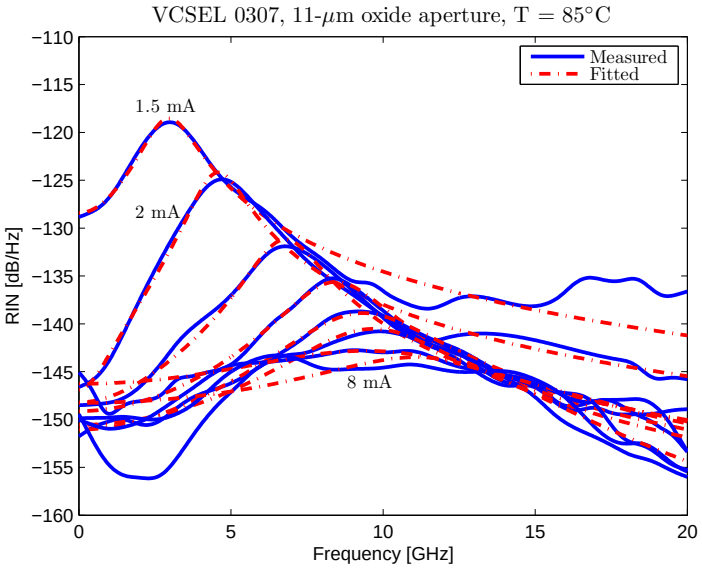


Figure 7.26: Fitting of RIN transfer function, for VCSEL with 11$\mu m$ oxide aperture diameter at85°$C$ operation.

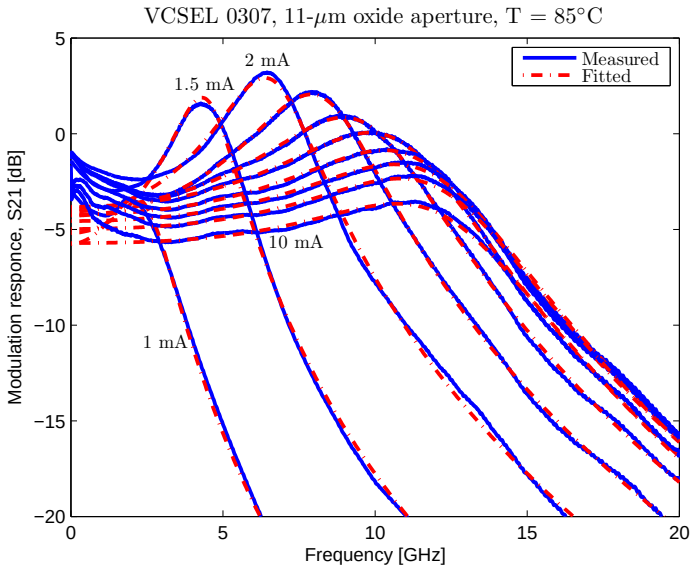


Figure 7.27: Fitting of modulation transfer function for small-signal modulation response, for VCSEL with 11$\mu m$ oxide aperture diameter at85°$C$ operation.

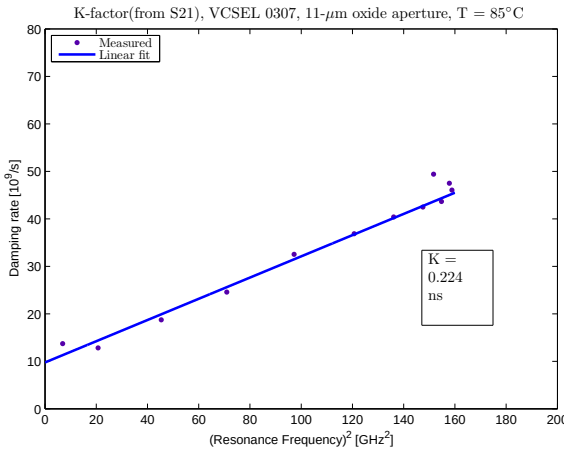


(a) K-factor from $S_{21}$

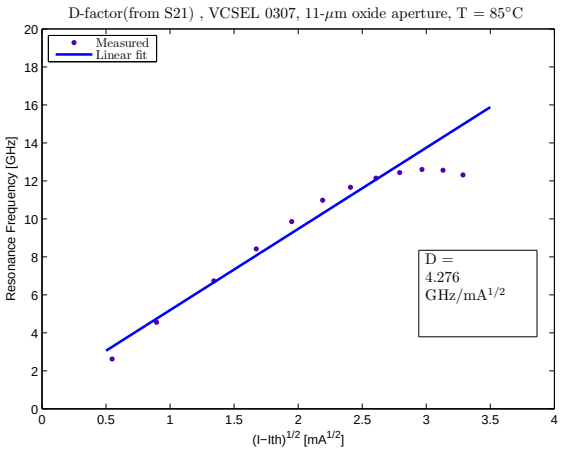


(b) D-factor from $S_{21}$

Figure 7.28: Extracted parameters from $S_{21}$measurement, for VCSEL with $11\mu m$ oxide aperture diameter at$85°C$ operation.

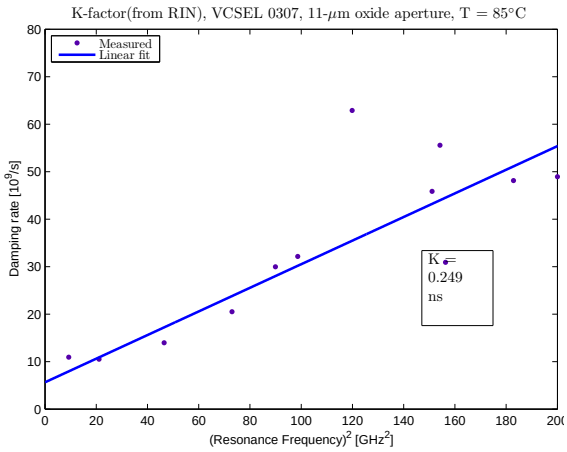


(a) K-factor from $RIN$

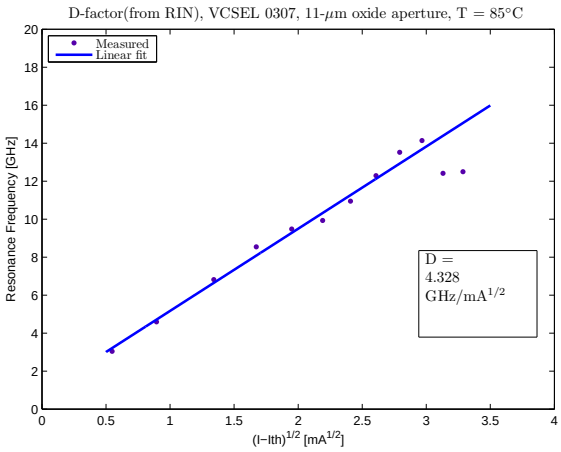


(b) D-factor from $RIN$

Figure 7.29: Extracted parameters from $RIN$ measurement, for VCSEL with $11\mu m$ oxide aperture diameter at$85°C$ operation.

### 7.4.8 $13\,\mu m$ oxide aperture at $85°C$

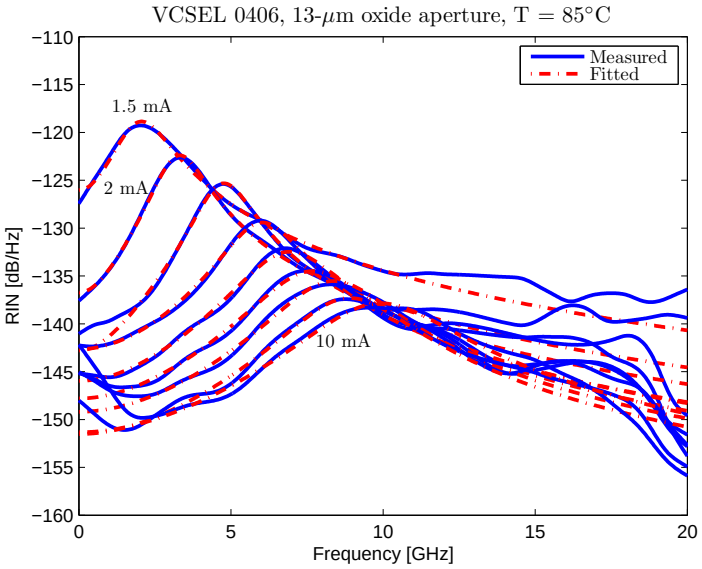


Figure 7.30: Fitting of RIN transfer function, for VCSEL with $13\mu m$ oxide aperture diameter at$85°C$ operation.

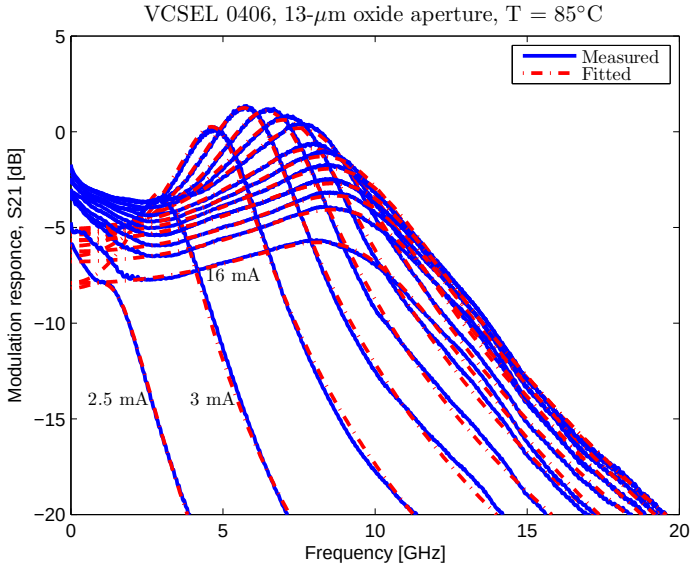


Figure 7.31: Fitting of modulation transfer function for small-signal modulation response, for VCSEL with $13\mu m$ oxide aperture diameter at$85°C$ operation.

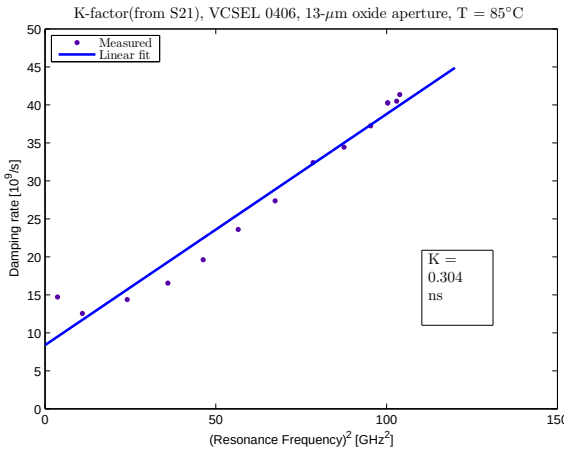


(a) K-factor from $S_{21}$

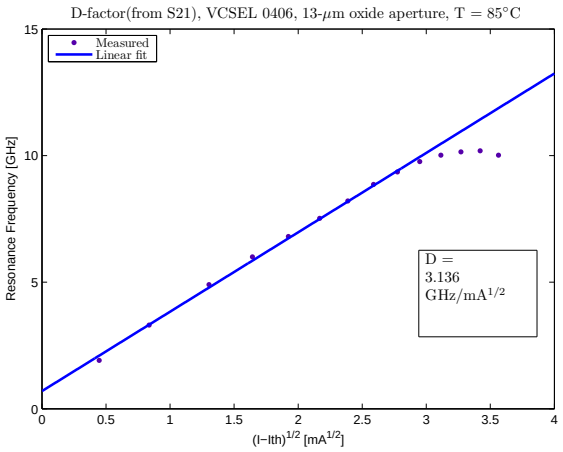


(b) D-factor from $S_{21}$

Figure 7.32: Extracted parameters from $S_{21}$measurement, for VCSEL with $13\mu m$ oxide aperture diameter at$85°C$ operation.

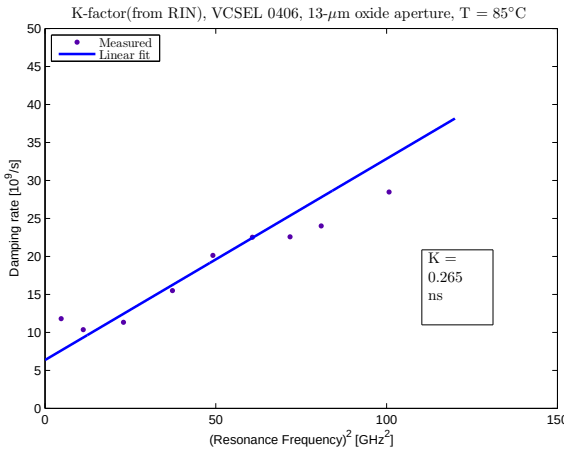


(a) K-factor from $RIN$

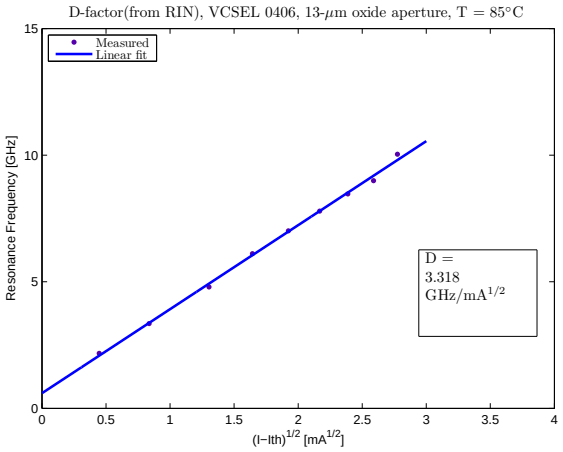


(b) D-factor from $RIN$

Figure 7.33: Extracted parameters from $RIN$ measurement, for VCSEL with $13\mu m$ oxide aperture diameter at$85°C$ operation.

### 7.4.9 Summary of the extracted parameters

In table 7.1, the final results of the extracted parameters from $RIN$ and $S_{21}$ at both RT and $85°C$ is summarized.

| VCSEL size $[\mu m]$ | 7 $(RT)$ | 9 $(RT)$ | 11 $(RT)$ | 13 $(RT)$ | 7 $(85°C)$ | 9 $(85°C)$ | 11 $(85°C)$ | 13 $(85°C)$ |
|---|---|---|---|---|---|---|---|---|
| $K_{S_{21}}[ns]$ | 0.259 | 0.144 | 0.159 | 0.162 | 0.241 | 0.200 | 0.224 | 0.304 |
| $K_{RIN}$ $[ns]$ | 0.080 | 0.145 | 0.108 | 0.149 | 0.068 | 0.335 | 0.249 | 0.265 |
| $D_{S_{21}}$ $[GHz/\sqrt{mA}]$ | 7.78 | 6.112 | 5.380 | 4.461 | 6.851 | 4.641 | 4.276 | 3.136 |
| $D_{RIN}$ $[GHz/\sqrt{mA}]$ | 7.13 | 5.813 | 5.435 | 4.638 | 6.462 | 4.430 | 4.328 | 3.318 |

Table 7.1: Extracted parameters from the $S_{21}$ and $RIN$ fittings.

Based on this table, we can observe that the $D$-factor decreases for VCSELs with a wider oxide aperture, however, the $K$-factor does not change significantly. Furthermore, the results at $85°C$ show smaller $D$-factor and rather large $K$-factors compared to the RT results.

# 8 Summary and future outlook

The work of this Master degree project has been both experimental and analytical. At the beginning of this report, the background theory necessary for conducting the work was discussed. The focus was mainly on the dynamic properties of VCSELs and therefore, on how relative intensity noise (RIN) can be defined for such device. Moreover, different properties of RIN have been discussed.

In the first experimental part of the project, relative intensity noise (RIN) was measured on state-of-the-art high-speed multi-mode 850-nm vertical-cavity surface-emitting lasers (VCSELs) intended for next generation short reach data communication standards. One measurement technique was chosen based on the advantages and the limitations for three different methods that were considered. Measurements were performed on devices with different current aperture diameters, at different bias currents, and at both room temperature (RT) and 85°C. It was shown that the RIN values obtained, are in most cases below the requirements of several different standards, e.g. for the future 32 Gb/s Fibre Channel (32GFC).

The second analysis part of the project dealt with extracting values of intrinsic dynamic laser parameters from RIN measurements and comparing to those extracted from corresponding $S_{21}$ measurements, which is the conventional method. Good agreement was found, and the pros and cons for the two extraction techniques are discussed. It was discussed that using RIN spectra for extraction of the parameters may be better since there is no effect from the electrical parasitics of the device. On the other hand, it was practically experienced that obtaining such RIN curves takes a lot more of energy and time, compared to the pretty straight-forward and fast $S_{21}$ measurements. Furthermore, it should be emphasized that the measured RIN curves will not be fitted equally well since the effect of reflections providing unwanted resonances are more pronounced in RIN plots. This problem is evident in the extracted values for the damping factor ($\gamma$), but not in the values for the resonance frequency ($f_r$). The reason is that the resonance frequencies (peaks in RIN spectra) are quite clear and therefore they will be fitted to the equation fairly well.

In future work, one should implement the setup for $RIN_{12}(OMA)$ that was discussed in Section 6.5.1 since many standards are specifying the required RIN values based on this new definition. This definition involves a more stressful and realistic condition for the laser, wherefore it can be regarded as a more useful value.

Furthermore, there are other techniques which do not require the usage of an ESA. They are considered as cheaper solutions for RIN characterization of semiconductor lasers and therefore, can have application where there is no real need to have very precise measurements, perhaps in industrial applications. It should be noted that there exist other techniques for measuring RIN that are based on optical spectrum analyzers (OSAa), RF power meters, or even oscilloscopes [10, 40].

# References


[1] L. A. Coldren and S. W. Corzine, *Diode lasers and photonics integrated circuits*, John Wiley & sons, New York, USA, 1995, p.221.

[2] P. Westbergh, *High speed vertical cavity surface emitting lasers for short reach communications*, Ph.D. Dissertation, Photonics Laboratory, Department of Microtechnology and Nanoscience (MC2), Chalmers University of Technology, Göteborg, 2011. ISBN/ISSN: 978-91-7385-527-3

[3] A. Abbaszadeh Banaeiyan, "One-chip integration of MEMS-Tunable VCSELs operating in the near-infrared regime", Thesis for Master of Science, Photonics Laboratory, Department of Microtechnology and Nanoscience (MC2), Chalmers University of Technology, Göteborg, 2011.

[4] A. Tomita and A. Suzuki, "A new density matrix theory for semiconductor lasers, including non-Markovian intraband relaxation and its application to nonlinear gain," *IEEE J. Quantum Electron.*, vol.27, no.6, pp.1630–1641, 1991.

[5] C. Carlsson, " Design and evaluation of vertical cavity surface emitting lasers for microwave applications", Ph.D. Dissertation, Photonics Laboratory, Department of Microtechnology and Nanoscience (MC2), Chalmers University of Technology, Göteborg, 2003. ISSN: 91-7291-351-7

[6] P. Westbergh, et al., "Speed enhancement of VCSELs by photon lifetime reduction", *Electronics Letters*, Vol. 46, No. 13, June 2010.

[7] P. Westbergh, et al., "40 Gbit/s error-free operation of oxide-confined 850-nm VCSEL", *Electronics Letters*, Vol. 46, No. 14, July 2010.

[8] P. Westbergh, et al., "Higher speed VCSELs by photon lifetime reduction", *Proceedings of SPIE* - The International Society for Optical Engineering. Vertical-Cavity Surface-Emitting Lasers XV; San Francisco, 26-27 January 2011.

[9] S. B. Healy, et al., " Active region design for high-speed 850-nm VCSELs", *IEEE J. Quantum Electron.,* vol. 46, no. 4, pp. 506–512, April 2010.

[10] "Lightwave signal analyzers measure relative intensity noise," Product Note 71400-1, *Agilent Technologies,* 2000.

[11] G. E. Obarski and P. D. Hale, "How to Measure Relative Intensity Noise in Lasers"; Laser Focus World 35(5): 273-277; May 99.

[12] R. Hui and M. O'Sullivan, *Fiber Optic Measurement Techniques*, Academic Press, Boston, USA, pp. 259–363, 2009.

[13] "Digital Communication Analyzer (DCA), Measure Relative Intensity Noise (RIN)," Product Note 86100-7, *Agilent Technologies,* May 2008.

[14] J. S. Gustavsson, J. Bengtsson, and A. Larsson, "Spatially dependent noise model for vertical-cavity surface-emitting lasers," *Quantum Electronics, IEEE Journal of* , vol.40, no.9, pp. 1163– 1176, Sept. 2004.

[15] Fiber optical communication course, Lecture 10: Optical amplifiers; Noise, OSNR, Sensitivity, Microtechnology and Nanoscience (MC2), Chalmers univeristy of technology, Göteborg, Sweden, 2010.

[16] C. M. Miller, "Intensity modulation and noise characterization of high-speed semiconductor lasers", *LTS, IEEE,* vol.2, no.2, pp.44–50, May 1991.

[17] G. P. Agrawal and N. K. Dutta, *Semiconductor Lasers*, Van Nostrand Reinhold, New York, pp.258-269, 1993.

[18] J. W. Law and G. P. Agrawal, "Mode-partition noise in vertical-cavity surface-emitting lasers", *Photonics Technology Letters, IEEE,* vol.9, Issue: 4, pp.437–439, April 1997.

[19] A. Valle and L. Pesquera, "Theoretical calculation of relative intensity noise of multimode vertical-cavity surface-emitting lasers", *Quantum Electronics, IEEE Journal of*, vol.40 Issue: 6, pp.597–606, June 2004.

[20] L.-G. Zei, S. Ebers, J.-R. Kropp, and K. Petermann, "Noise performance of multimode VCSEL", *Lightwave Technology, Journal of*, vol.19, Issue: 6, pp.884–892, June 2001.

[21] K. H. Hahn, M. R. Tan and S. Y. Wang, "Intensity noise of large area vertical cavity surface emitting lasers in multimode optical fiber links", *Electron. Lett.*, vol. 30, pp. 139–140, 1994.

[22] J. L. Gimlett and N. K. Cheung, "Effects of phase-to-intensity noise conversion by multiple reflections in Gigabit-per-second DFB laser transmission systems", *J. Lightwave Technol.* Vol.7, pp.888–895, 1989.

[23] R. W. Tkach and A. R. Chraplyvy, "Regimes of feedback effects in 1.5-$\mu m$ DFB lasers", *J. Lightwave Technol.* LT4, pp.1655–1661, 1986.

[24] J. Wang and K. Petermann, "Small signal analysis for dispersive optical fiber communiation systems", *J. Lightwave Technol.* Vol.10 (No. 1), pp.96–100, 1992.

[25] D. Derickson , *Fiber Optic Test and Measurement*, Prentice-Hall, New Jersey, pp.269, 1998.

[26] [Online]. Available: http://en.wikipedia.org/wiki/Amplitude_modulation#Modulation_index, Downloaded on Feb. 15, 2012.

[27] "Impact of Transmitter RIN on Optical Link Performance," Application Note 3470, *Maxim*, Feb 2005. [Online]. Available: http://www.maxim-ic.com/app-notes/index.mvp/id/3470

[28] D. Cunningham and W. G. Lane, *Gigabit Ethernet Networking*, Mcmillan Technical Publishing, Indianapolis, 1999, pp.301–336.

[29] G. P. Agrawal, *Fiber Optic Communication Systems*, Second Edition, John Wiley, New York, pp.170–172, 1997.

[30] J. S. Gustavsson, *personal communication.*

[31] C. M. Miller and L. F. Stokes, "Measurement of laser diode intensity noise below the shot noise limit", Boulder, CO: *NIST Symp. on Optical Fiber Measurements*, 1990.

[32] M. Movassaghi, "Characterization and Modeling of Erbium-Doped Fiber Amplifiers and Impact of Fiber Dispersion on Semiconductor Laser Noise," in Department of Electrical Engineering and Computer Science, vol. Doctor of Philosophy Vancouver: University of British Columbia, 1999.

[33] J. Poette, P. Besnard, L. Bramerie and J. Simon, "Highly-sensitive measurement technique of relative intensity noise and laser characterization", *Proc. of SPIE*, Vol. 6603, 66031R-10, 2007.

[34] M. C. Cox, N. J. Copner, and B. Williams, "High sensitivity precision relative intensity noise calibration standard using low noise reference laser source", *Science, Measurement and Technology, IEE Proceedings* - , vol.145, no.4, pp.163-165, Jul 1998.

[35] S. M. Vaezi-Nejad, M. Cox and N. Coope, "Novel instrumentation for measurement of relative intensity noise", *Transactions of the Institute of Measurement and Control,* 15 April 2011. [Online]. Available: http://tim.sagepub.com/content/early/2011/04/12/0142331211399330

[36] G. E. Obarski and J. D. Splett, "Measurement Assurance Program for the Spectral Density of Relative Intensity Noise of Optical Fiber Sources near 1550 nm"; *NIST* SP 250-57, 90 pp, Sep 2000.

[37] "Agilent Spectrum Analysis Basics," Application Note 150, Chapter 2, *Agilent Technologies,* 2006.

[38] A. Quirce, A. Valle, C. Gimenez, and L. Pesquera, "Intensity Noise Characteristics of Multimode VCSELs", *Lightwave Technology, Journal of*, vol.29, Issue: 7, pp.1039–1045, 2011.

[39] A. Larsson, "Advances in VCSELs for Communication and Sensing," *Selected Topics in Quantum Electronics, IEEE Journal of* , vol.17, no.6, pp.1552–1567, Nov.-Dec. 2011.

[40] R. Johnson, "Experiments in Measuring Laser RIN with an Oscilloscope", *Finisar*, Oct. 2011. [Online]. Available: ftp://ftp.t10.org/t11/document.11/11-405v0.pdf

[41] "Final report on system specifications and standards", Deliverable 5.11 of the European project VISIT, 2011. [Online]. Available: http://www.visit.tu-berlin.de/fileadmin/f23/D5.11_PU.pdf

[42] "Fibre Channel Methodologies for Signal Quality Specification - MSQS Rev 0.2", Chapter 7. [Online]. Available: http://www.t11.org/ftp/t11/pub/fc/msqs/09-263v1.pdf

[43] "IEEE 802.3ba™ ", Amendment 4 to IEEE 802.3™, Chapter 86, 2010. [Online]. Available: http://standards.ieee.org/about/get/802/802.3.html

[44] M. Dudek, "OMA Proposal", *Cielo Communications*, November 2000. [Online]. Available: http://www.ieee802.org/3/ae/public/nov00/dudek_2_1100.pdf

[45] "Spectrum Analyzer Measurements and Noise," Application Note 1303, *Agilent Technologies,* 2000.

[46] P. Westbergh, J. S. Gustavsson, B. Kögel, A. Haglund, and A. Larsson, "Impact of Photon Lifetime on High-Speed VCSEL Performance," *Selected Topics in Quantum Electronics, IEEE Journal of* , vol.17, no.6, pp.1603–1613, Nov.-Dec. 2011.

# Appendix A

# Correction factor in noise measurements using ESA

The measured level at the output of a spectrum analyzer must be manipulated in order to represent the input spectral noise density which we desire to measure. These corrections are due to some under-response or over-response due to some mechanisms. At first, the block diagram of a typical spectrum analyzer should be noticed which is depicted in Fig. A.1.

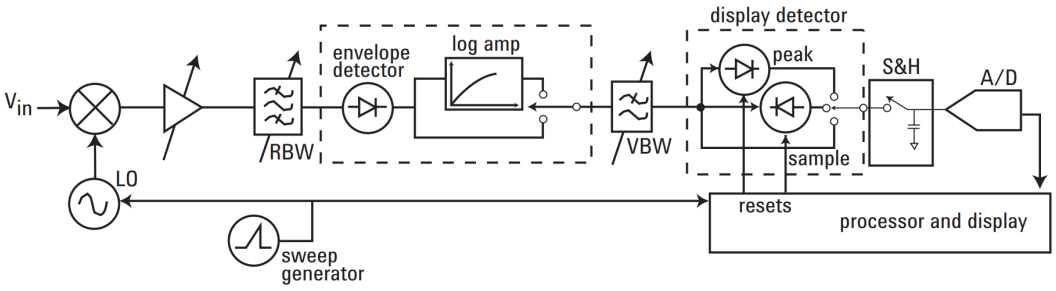


Figure A.1: A simplified block diagram of a spectrum analyzer [45]

For noise measurements, the power of the noise is the parameter that we want to measure usually with a spectrum analyzer. The power is the "heating value" of the signal, which, mathematically, is the average of $V^2/R$, where $R$ is the impedance of the signal and $V$ is its instantaneous voltage. In a spectrum analyzer, the average of the envelope voltage is found using the envelope detector and the value is consequently squared and divided by $R$. There is, however, a consistent under-measurement of noise from squaring the average instead of averaging the square; this under-measurement is 1.05 dB.

The second contribution to the correction factor comes from the fact that, spectrum analyzers are most commonly used in their logarithmic ("log") display mode, in which the vertical axis is calibrated in decibels. When the average power of the noise is expressed in decibels, the logarithm of that average power is normally computed. However, the output of the log scale is averaged in spectrum analyzers. The log of the average is not equal to the average of the log. Therefore, it is found that that log processing causes an under-response to noise of 2.51 dB rather than 1.05 dB (which was in linear scale case).

Finally, the third mechanism due to the non-ideality of the resolution bandwidth (RBW) of spectrum analyzers. The ideal RBW filter has a flat passband and infinite attenuation outside the passband. In Fig. A.2, the power gain (the square of the voltage gain) of the RBW filter versus frequency is illustrated. If we assume that noise of flat power spectral density passes through the passband filter, the response of such filter to noise is the same as the response of a rectangular filter with the same maximum gain and the same area under their curves. The width of such a rectangular filter is the "equivalent noise bandwidth" of the RBW filter. Depending on the type of filter which is used as the RBW filter, the ratio of the equivalent noise bandwidth to the 3-dB bandwidth is given. Most spectrum analyzers use four-pole synchronously tuned filters

for their RBW filters, which give the ratio of 1.128 or 0.52 dB. This ratio is the amount of the over-response which has to be compensated [45].

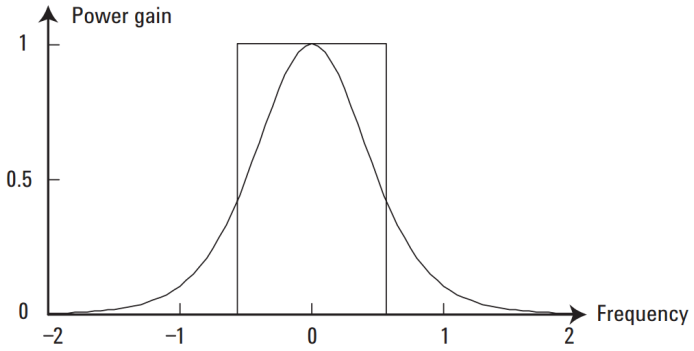


Figure A.2: The power gain versus frequency of an RBW filter which can be modeled by a rectangular filter with the same area and peak level, and a width of the ”equivalent noise bandwidth”. [45]

## The noise marker function

As discussed above, manipulation of the measured level at the output of a spectrum analyzer is required. This manipulation involves three factors, which should be added in decibel units:

1. Under-response due to voltage envelope detection (add 1.05 dB) or log-scale repose (add 2.51 dB).

2. Over-response due to the ratio of the equivalent noise bandwidth to the 3-dB bandwidth of the RBW filter (subtract typically 0.52 dB– depending on the filter type)

The noise marker function is a feature that is available in typical spectrum analyzers. This function calculates the impact of these two factors and adds the suitable correction factor to the measured data. The final value of the correction factor in the case of using the log-scale will be 2 dB which should be added to the measured values.

Moreover, this function delivers some more features which are suitable for typical noise measurements. It normalizes the output values to 1–Hz bandwidth, where the units are typically dBm/Hz. A further operation of the noise marker is to average 32 measurement cells centered around the marker location in order to reduce the variance of the result [45].